OAK RIDGE NATIONAL LABORATORY LIBRARY
3 4456 0004785 7

ORNL/Sub/84-95128/3

140 GHz GYROTRON DEVELOPMENT PROGRAM

QUARTERLY REPORT NO. 3

OCTOBER THROUGH DECEMBER 1984

FUSION ENERGY DIVISION LIBRARY
MAR 17 86

K.L. FELCH, R.E. BIER, L.J. CRAIG, L.J. FOX, B.D. GAISER,
G. HU, H.E. HUEY, R.L. IVES, H.R. JORY, P.I. REYSNER,
A. SALOP, S.T. SPANG, B.C. STOCKWELL

Report Prepared by
VARIAN ASSOCIATES, INC.
611 HANSEN WAY
PALO ALTO, CA 94303

FUSION ENERGY DIVISION LIBRARY

under
SUBCONTRACT PURCHASE ORDER NO. 55Y-95128C

for

OAK RIDGE NATIONAL LABORATORY
OAK RIDGE, TENNESSEE 37831

Operated by
MARTIN MARIETTA ENERGY SYSTEMS, INC.

for

U. S. DEPARTMENT OF ENERGY
UNDER CONTRACT NO. DE-AC05-84OR21400

Printed in the United States of America. Available from:
National Technical Information Service
U.S. Department of Commerce
5255 Port Royal Road, Springfield, Virginia 22161
NTIS price codes — Printed Copy: A99 Microfiche A01

This report was prepared as an account of work sponsored by an agency of the United States Government. Neither the United States Government nor any agency thereof, nor any of their employees, makes any warranty, express or implied, or assumes any legal liability or responsibility for the accuracy, completeness, or usefulness of any information, apparatus, product, or process disclosed, or represents that its use would not infringe privately owned rights. Reference herein to any specific commercial product, process, or service by trade name, trademark, manufacturer, or otherwise, does not necessarily constitute or imply its endorsement, recommendation, or favoring by the United States Government or any agency thereof. The views and opinions of authors expressed herein do not necessarily state or reflect those of the United States Government or any agency thereof.

ORNL/Sub/84-95128/3

140 GHz GYROTRON DEVELOPMENT PROGRAM

QUARTERLY REPORT NO. 3

OCTOBER THROUGH DECEMBER 1984

K.L. FELCH, R.E. BIER, L.J. CRAIG, L.J. FOX, B.D. GAISER,
G. HU, H.E. HUEY, R.L. IVES, H.R. JORY, P.I. REYSNER,
A. SALOP, S.T. SPANG, B.C. STOCKWELL

Report Prepared by
VARIAN ASSOCIATES, INC.
611 HANSEN WAY
PALO ALTO, CA 94303

under
SUBCONTRACT PURCHASE ORDER NO. 55Y-95128C

for
OAK RIDGE NATIONAL LABORATORY
OAK RIDGE, TENNESSEE 37830

Operated by
MARTIN MARIETTA ENERGY SYSTEMS, INC.
for
U.S. DEPARTMENT OF ENERGY
UNDER CONTRACT NO. DE-AC05-83OR21400

OAK RIDGE NATIONAL LABORATORY LIBRARY
3 4456 0004785 7

TABLE OF CONTENTS

Section		Page
I.	INTRODUCTION	1
II.	ELECTRON GUN	3
III.	INTERACTION CIRCUIT	4
	A. Cavity Design - Electrical	4
	B. Cavity Design - Cooling	9
	C. Beam Tunnel Considerations	29
IV.	COLLECTOR	36
	A. Output Taper Design	36
V.	OUTPUT WINDOW DESIGN	37
	A. Double-Disc Window	37
	B. Double-Dish Windows	57
VI.	SUPERCONDUCTING SOLENOID MAGNET SYSTEM	58
VII.	140 GHz COMPONENTS, DIAGNOSTICS AND PROTECTIVE DEVICES	62
	A. Waterload	62
	B. Infrared Diagnostics	62
	C. Mode Filter	62
	D. Arc Detector/Frequency Sampler	63
	E. Directional Coupler	63
VIII.	PROGRAM SCHEDULE AND PLANS FOR NEXT QUARTER	65

LIST OF ILLUSTRATIONS

Figure		Page
1.	Mode Plot of a TE_{021}/TE_{031} Complex Cavity	6
2.	Mode Plot of TE_{031} Simple Cavity Design No. 1, When Excited at the Resonant Frequency of the Cavity, 140.10 GHz	7
3.	Mode Conversion and Back-rf Leakage versus Frequency for Simple Cavity Design #1	8
4.	Mode Conversion and Back-rf Leakage vs Frequency for Simple Cavity Design No. 2	10
5.	Power Density Profile for TE_{031} Simple Cavity Design No. 1	11
6.	Temperature Profile Along Inner Wall of Simple Cavity for 10 kW CW Output	12
7.	Temperature Profile Along Inner Wall of Simple Cavity for 50 kW CW Output	13
8.	Temperature Profile Along Cooling Channel Surface of Simple Cavity for 50 kW CW Output	15
9.	Temperature Profile Along Cavity Inner Wall of Simple Cavity for 50 kW CW and 2.5 kW Beam Interception	16
10.	Power Density Profile for TE_{021}/TE_{031} Complex Cavity for 100 KW CW Operation	17
11.	Temperature Profile Along the Inner Wall of the Complex Cavity Made from OFHC Copper	19
12.	Temperature Profile Along Cooling Channel Surface of Complex Cavity Made from OFHC Copper	20
13.	Temperature Profile Along Inner Wall of Complex Cavity Made from AL-15 Copper	21
14.	Temperature Profile Along Cooling Channel Surface of Complex Cavity Made from AL-15 Copper	22
15.	Stress Profile Along Inner Wall of Complex Cavity Made from OFHC Copper	23
16.	Stress Profile Along Cooling Channel Surface of Complex Cavity Made from OFHC Copper	24
17.	Stress Profile Along Inner Wall of Complex Cavity Made from AL-15 Copper	25

LIST OF ILLUSTRATIONS (Cont'd)

18. Stress Profile Along Cooling Channel Surface of Complex Cavity Made from AL-15 Copper 26

19. Displacement Profile Along the Inner Wall of Complex Cavity Made from OFHC Copper 27

20. Displacement Profile Along the Inner Wall of the Complex Cavity Made from AL-15 Copper 28

21. Axial Temperature Profile Along Beam Tunnel ID for 1 kW Absorbed Power in Ceramic Ring 31

22. Axial Hoop Stress Profile at the Radius of Maximum Tensile Stress for 1 kW Absorbed Power in Ceramic Ring 32

23. Axial Temperature Profile along Beam Tunnel ID for 250 W Absorbed Power in Ceramic Ring 33

24. Axial Hoop Stress Profile at the Radius of Maximum Tensile Stress for 250 W Absorbed Power in the Ceramic Ring 34

25. Validation of 3-D Window Structural Model: Finite Element Model for 2-D Analysis 38

26. Validation of 3-D Window Structural Model: Finite-Element Model for 3-D Brick Elements (3 Elements Across Thickness) 39

27. Validation of 3-D Window Structural Model: Finite-Element Model for 3-D Shell Elements (1 Element Across Thickness) 40

28. Validation of 3-D Window Structural Model: Calculated Window Deflection for 2-D Flat Brick Elements 41

29. Validation of 3-D Window Structural Model: Calculated Window Deflection for 3-D Brick Elements 42

30. Validation of 3-D Window Structural Model: Calculated Window Deflection for 3-D Shell Elements 44

31. Finite Element 3-D Model for Thermal Analysis of the 140 GHz Double-Disc Window 45

32. Double-Disc Window 3-D Analysis: Temperature Profile From Center to Inlet for the Vacuum Side of the Window, 100 kW CW Operation 46

LIST OF ILLUSTRATIONS (Cont'd)

33. Double-Disc Window 3-D Analysis: Temperature Profile From Center to Inlet for the Coolant Side of the Window, 100 kW CW Operation 47

34. Axial Deformation of a 3-D Finite Element Structure for the 140 GHz Window With Pressure Load Only 49

35. Double-Disc Window 3-D Analysis: Displacement Profile From Center to Inlet for the Vacuum Side of the Window, Pressure Load Only 50

36. Double-Disc Window 3-D Analysis: Displacement Profile From Center to Outlet for the Vacuum Side of the Window, Pressure Load Only 51

37. Double-Disc Window 3-D Analysis: Stress Profile From Center to Inlet for the Vacuum Side of the Window, Pressure Load Only 52

38. Double-Disc Window 3-D Analysis: Stress Profile from Center to Inlet for the Coolant Side of the Window, Pressure Load Only 53

39. Double-Disc Window 3-D Analysis: Deflection Profile from Center to Inlet for the Vacuum Side of the Window, 100 kW CW Operation 54

40. Double-Disc Window 3-D Analysis: Stress Profile from Center to Inlet for the Vacuum Side of the Window, 100 kW CW Operation 55

41. Double-Disc Window 3-D Analysis: Stress Profile from Center to Inlet for the Coolant Side of the Window, 100 kW CW Operation 56

42. 140 GHz Magnet Dewar Layout 59

43. Superconducting Solenoid Manufacturing Process 61

44. Milestone Chart 66

ABSTRACT

The objective of this program is to develop a gyrotron oscillator capable of producing 100 kW of CW power at 140 GHz. An analysis of various characteristics of the interaction circuit, collector and output window is presented for the first two experimental tubes, Experimental Tube 1 and Preprototype Tube 1. The final coil configurations for the two superconducting magnet systems are summarized. Various aspects relating to the design of 140 GHz gyrotron components, diagnostics, and protective devices are discussed.

I. INTRODUCTION

The objective of this program is to develop a gyrotron oscillator designed to produce 100 kW of CW output power at 140 GHz. Output mode purity, tube reliability, and punctual completion of the prototype tubes, magnets, and components are the major considerations underlying the design decisions for the 140 GHz gyrotron. Output efficiency and logistical aspects, such as tube length and cooling requirements, are additional secondary concerns of the tube design.

The 140 GHz gyrotron will be designed to generate microwaves in the TE_{03} mode in circular waveguide. The interaction circuit will consist of a simple TE_{031} cavity or TE_{021}/TE_{031} complex cavity. In addition, tests employing the TE_{231} mode in a simple cavity will be performed as a backup approach to the circular electric mode interaction. The electron beam will have a perpendicular to parallel velocity ratio of between 1.5 and 2.0 and will be located at the second radial maximum of the TE_{031} mode. The beam will be generated by a magnetron injection electron gun and the 56 kG magnetic field required for the gyrotron interaction will be provided by a superconducting magnet.

During this quarter, the output mode purity and back-rf leakage for a TE_{021}/TE_{031} complex cavity design was analyzed. Several modifications to the original design have enabled a reduction in the output mode conversion to 2.5% with 1.5% back-rf leakage. In addition, the two simple TE_{031} cavity designs, chosen for use on the first experimental tube, were analyzed in the same manner and gave similar results. Thermomechanicial analyses of both the complex TE_{021}/TE_{031} and simple TE_{031} designs were performed to validate the cooling designs for the cavities.

Considerations for the design of the beam tunnel between the electron gun and cavity were investigated. These design considerations include:

1) the capability of safely absorbing rf power leaking back from the cavity;

2) proper beam propagation from the gun to the circuit without interception or excessive potential depression and;

3) the prevention of resonant interactions with the beam in the beam tunnel.

The final design for a pure mode uptaper between the cavity and the collector for the second experimental tube, Preprototype Tube 1, was completed. The design is capable of transporting the TE_{03} mode from the cavity to the collector with only 1.7% mode conversion to other TE_{0n} modes.

A three-dimensional, finite-element model of the double-disc output window was created and used to calculate the temperatures and stresses in the window. Results of this analysis indicate that the temperature and stress in the window appear to be within acceptable limits for reliable tube operation.

Two magnet designs employing two main magnet coils have been finalized and are currently being fabricated by two different vendors. Progress on the construction of the two magnets is being monitored quite closely to ensure timely delivery of the systems. Other gyrotron components, diagnostics, and protective devices required for testing the first experimental tube have been designed and readied for manufacture. The design for a test directional coupler at 35 GHz has been modified slightly to facilitate its fabrication.

II. ELECTRON GUN

The primary electron gun design to be incorporated in the first tube, Experimental Tube 1, is currently being assembled. Analysis of this design was completed during the previous reporting period.[1] A second electron gun design was also analyzed in the previous quarter and will be employed as a back-up to the primary gun design.[1] A gun of this design was constructed for use in gyrotron experiments at 140 GHz at the Massachusetts Institute of Technology, though it was operated at values of beam voltage and beam current that differ slightly from the values to be used in the present 140 GHz gyrotrons.[2] A gun of the back-up design is being constructed and will be completed in time for use on Preprototype Tube 1 if experiments on Experimental Tube 1 indicate that a change from the primary design is warranted.

III. INTERACTION CIRCUIT

A. CAVITY DESIGN - ELECTRICAL

During this quarter, work continued on the analysis of the back-rf leakage and output mode purity of the TE_{021}/TE_{031} complex cavity design to be used on the second experimental tube, Preprototype Tube 1. In addition, a similar analysis was performed on the two TE_{031} simple cavity designs to be used on the first tube, Experimental Tube 1, and its subsequent rebuild. Both analyses were carried out using the finite-element computer code OPENCAV.

Back-rf Leakage and Mode Purity Analysis of TE_{021}/TE_{031}-Complex Cavity Design

As discussed in a previous report,[1] the TE_{021}/TE_{031}-type complex cavity is susceptible to both power leakage from the cavity back toward the gun and impurity of the output TE_{03} waveguide mode. Design goals of less than 1% back-rf leakage and less than 2% non-TE_{03} mode output have been specified for the present 140 GHz, 100 kW CW tube development. Back-rf leakage was set at less than 1% so that less than 1 kW of power would need to be absorbed in the beam tunnel between the cavity and the gun. This facilitates cooling in the beam tunnel. The beam tunnel must absorb the power to avoid beam instabilities in the gun and beam tunnel regions. Our goal of less than 2% impurity in the output mode is consistent with the overall tube requirement of 95% output mode purity. As we will discuss in Section IV, the taper from the cavity to the collector contributes an additional 2% of mode conversion, so that a total mode conversion of 95% is possible with 2% impurity at the output of the cavity.

In previous calculations, values of 1.3% and 6% were obtained for the rf leakage and mode impurity, respectively, of a TE_{021}/TE_{031} cavity design.[1] However, this calculation did not allow for an iris at the output of the TE_{031} section. An iris is required to obtain the desired loaded Q of the circuit. More recent calculations have included an iris which yields the desired loaded Q of 600 - 800. Thus far, the best iteration of this design

results in back-rf leakage of 1.5% and an output mode impurity of 2.5%. An OPENCAV plot of this design is shown in Figure 1. Plotted in the figure are lines of constant rf electric field. In analyzing the plot, evidence of some back-rf leakage from the TE_{021} section toward the gun is visible. The iris is shown at the exit of the TE_{031} section, in the transition zone between the standing wave in the cavity and the traveling wave in the uptaper. The output mode purity appears quite good in the plot, though small amounts of mode conversion are hard to identify in such a plot. The cavity is still being modified in order to reach the design goals for back-rf leakage and output mode purity, though the 1.5% and 2.5% values already obtained are probably adequate.

Back-rf Leakage and Mode Purity Analysis of TE_{031}—Simple Cavity Designs

The basic design of the TE_{031} cavities to be used in the first tube, Experimental Tube 1, has been discussed in a previous report.[3] That early analysis included both small-signal and large-signal interaction calculations and cavity wall-loading considerations. In light of the above analysis of the TE_{021}/TE_{031} complex cavity design, which indicates that non-negligible amounts of back-rf leakage and output mode impurity can be present, a similar analysis was performed for the two chosen TE_{031} simple-cavity designs.

An OPENCAV plot of the lines of constant cavity electric field for Design #1 is shown in Figure 2. Here we see that the TE_{031} mode in the cavity appears to be relatively pure with a little evidence of back-rf leakage toward the electron gun. In Figure 3, we have plotted the percentage of back-rf leakage and mode impurity in the output wave as a function of frequency for Design #1. Here we observe that output mode conversion and back-rf leakage reach minimum values near the resonant frequency of the cavity. At the resonant frequency, 1.3% of the power in the cavity leaks back toward the gun, while 2.6% of the output power is in the TE_{01} and TE_{02} modes rather than the desired TE_{03} mode. A similar plot of back-rf leakage and output mode conversion for TE_{031} Design #2 is shown

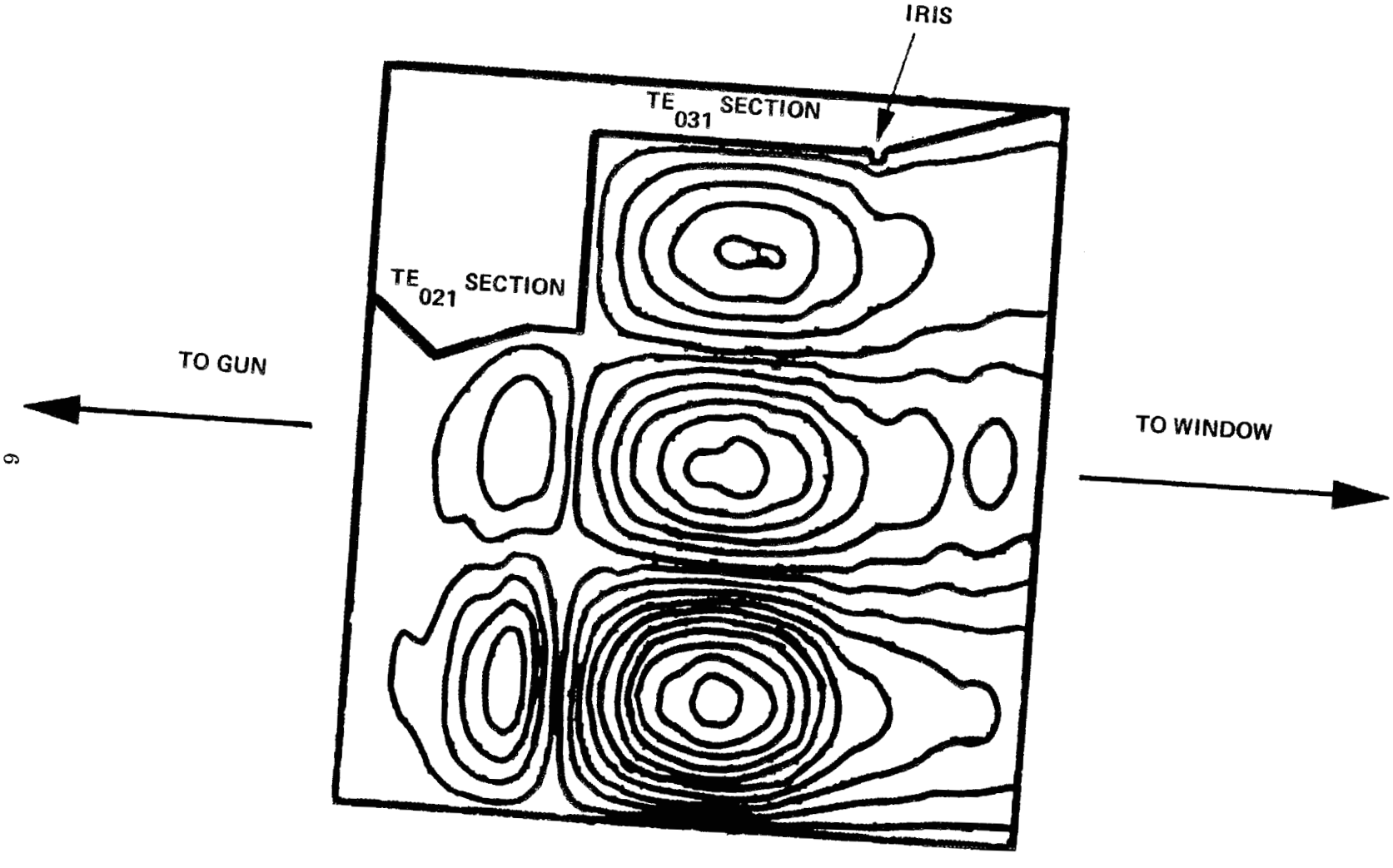

Figure 1. Mode plot of a TE_{021}/TE_{031} complex cavity. In this design, back-rf leakage and output mode conversion have been reduced to 1.5% and 2.5%, respectively.

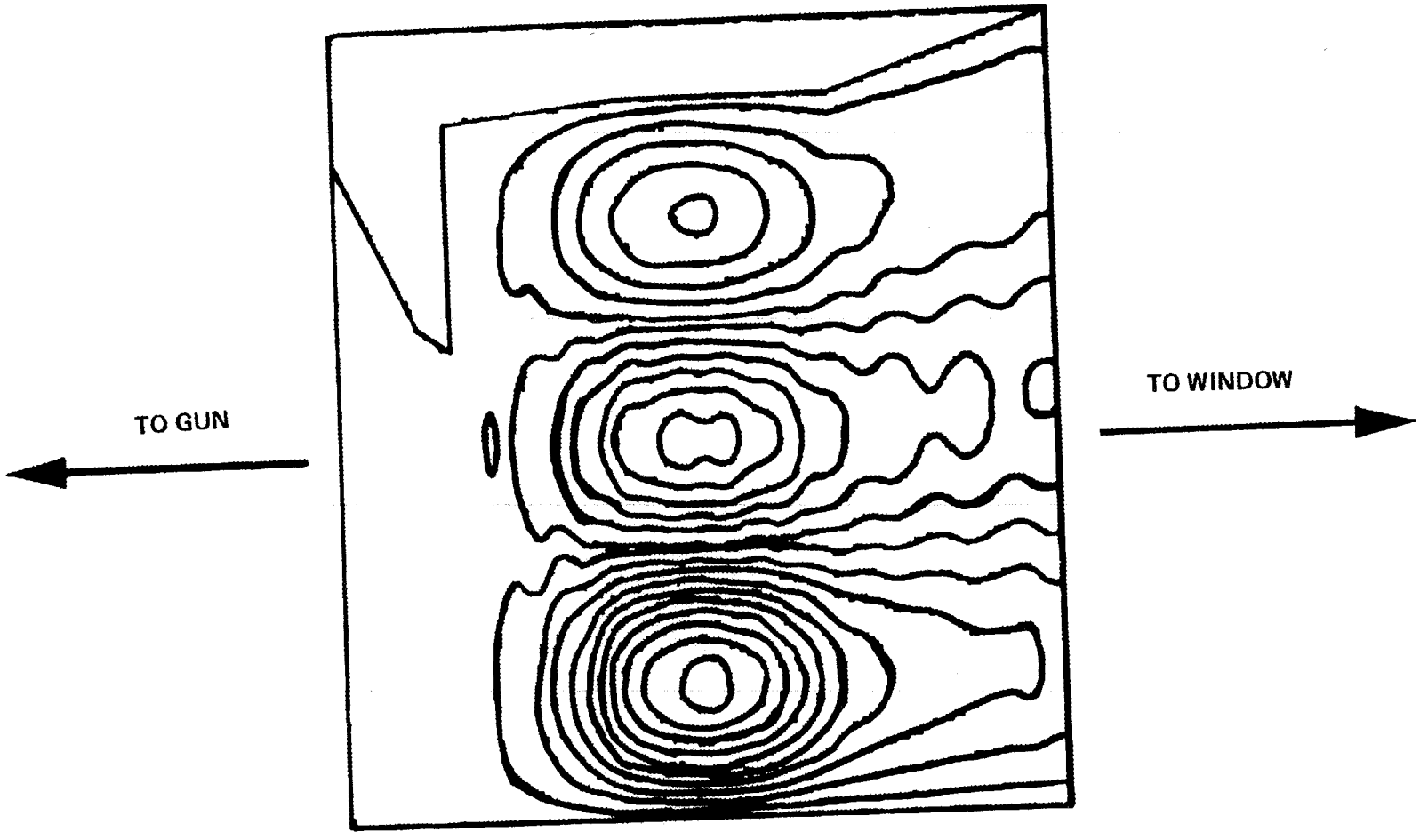

Figure 2. Mode plot of TE_{031} Simple Cavity Design No. 1, when excited at the resonant frequency of the cavity, 140.10 GHz.

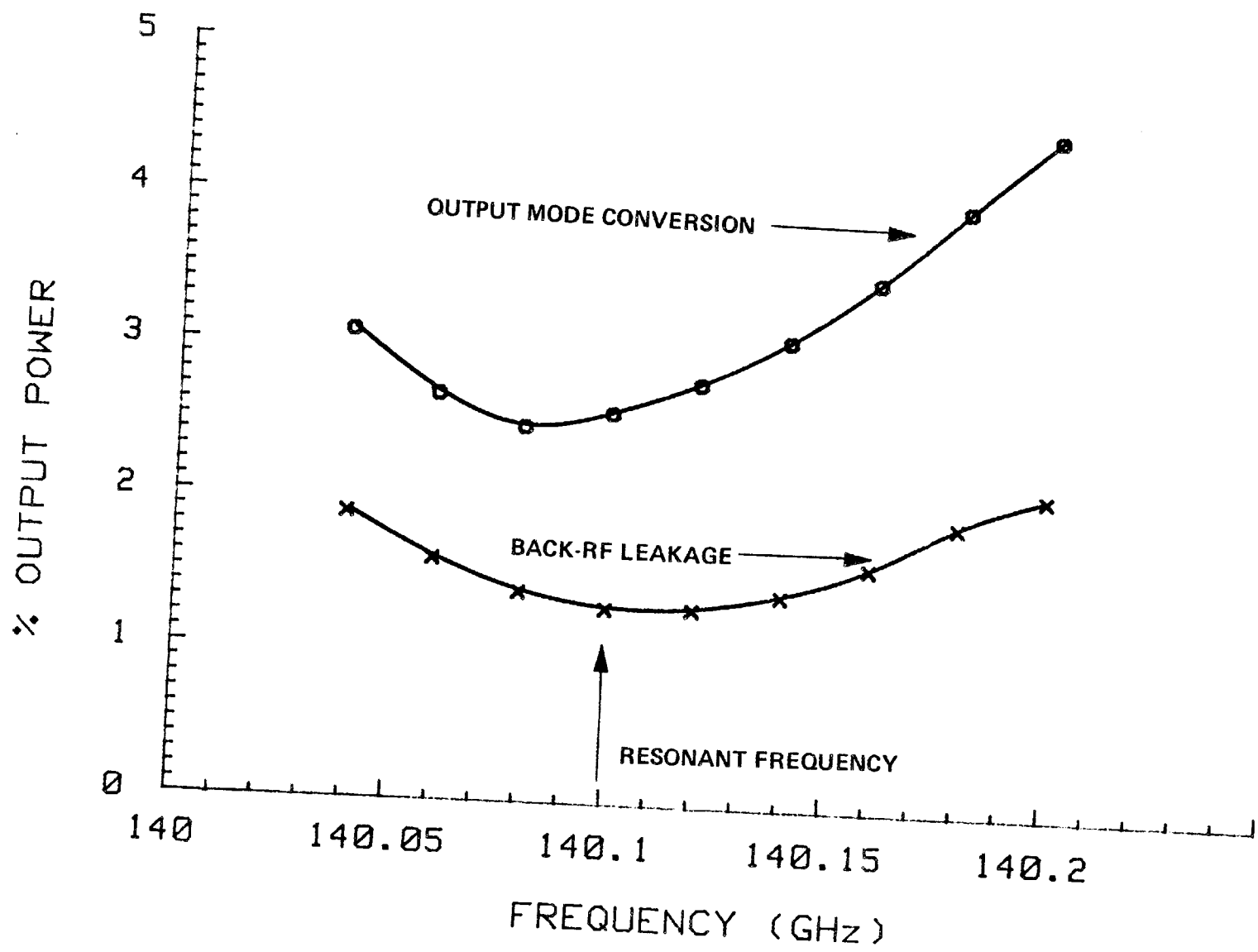

Figure 3. Mode conversion and back-rf leakage vs frequency for Simple Cavity Design No. 1.

in Figure 4. This design, which possesses a higher value of Q_L than Design #1, has similar values of back-rf leakage and output mode impurity.

As noted earlier in our discussion of the TE_{021}/TE_{031} cavity analysis, values of less than 1% back-rf leakage and less than 2% output mode impurity are the design goals for any of the 140 GHz cavity designs. Though the present designs exhibit performance near these values, small modifications in the cavity designs, similar to those being investigated for the TE_{021}/TE_{031} cavity, may improve these cavity characteristics without changing the interaction performance of the circuit.

B. CAVITY DESIGN - COOLING

Simple Cavity Design

One of the simple TE_{031} cavity designs to be tested in Experimental Tube 1 (Design #1) was modeled, and the resulting temperatures, stresses and displacements were calculated for CW power levels of 10 and 50 kW. The power density profile for this cavity is shown in Figure 5. The parameters used for these calculations are as follows:

Material	OFHC Copper
Tube Power	10 kW or 50 kW
Peak Power Density	0.4 kW/cm^2 or 2.5 kW/cm^2
Cooling Fluid	Oxygen-free, deionized water
Coolant Velocity	30 ft/sec
Coolant Inlet Pressure	150 psi
Reynold's Number	18,600

Figure 6 gives the temperature profile along the cavity inner wall for the 10 kW CW case. The peak temperature is $47^{o}C$. Figure 7 gives the temperature profile along the cavity inner wall for the 50 kW CW case. There the peak temperature is $162^{o}C$. These are operating temperatures with a generous safety margin.

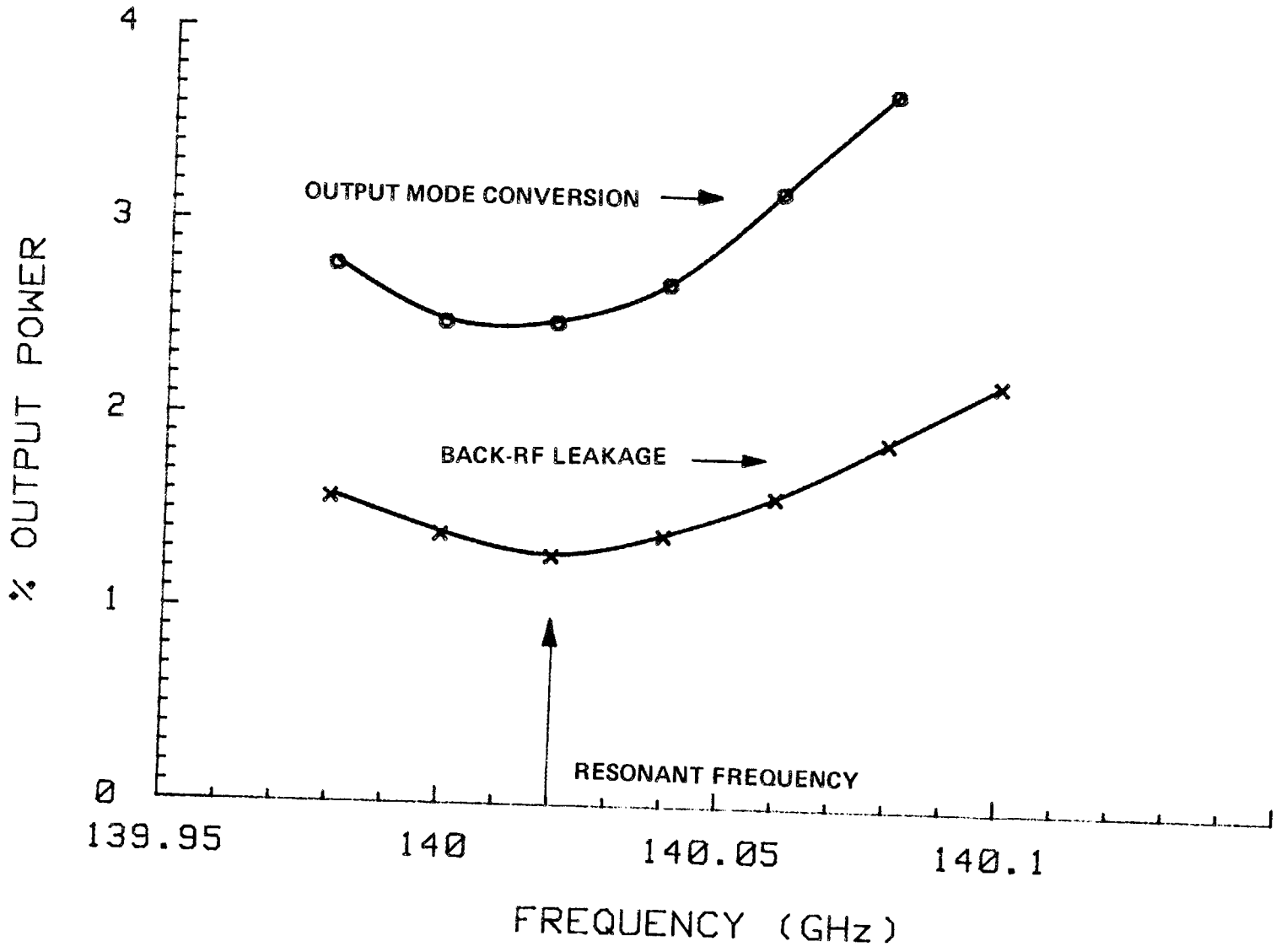

Figure 4. Mode conversion and back-rf leakage vs frequency for Simple Cavity Design No. 2.

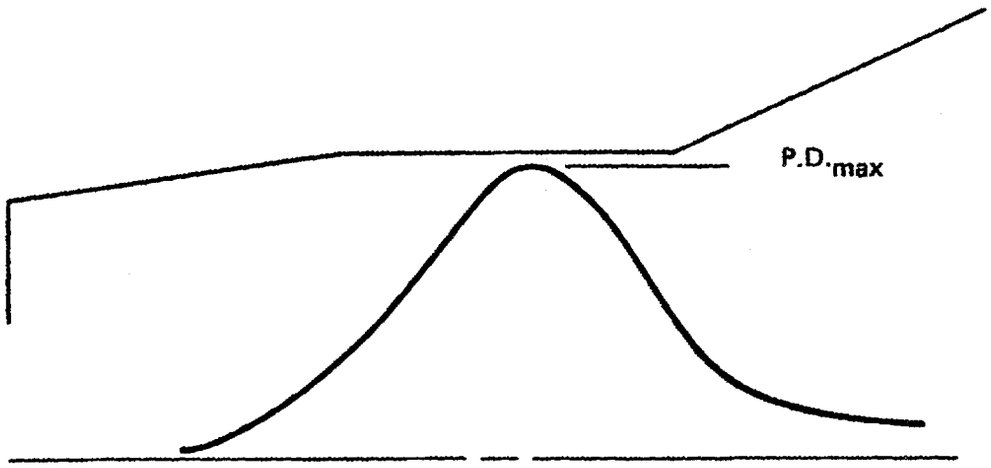

$P.D._{max} = 0.4^{*}\frac{KW}{cm^2}$ AT 10 KW CW OUTPUT

$P.D._{max} = 2.5^{*}\frac{KW}{cm^2}$ AT 50 KW CW OUTPUT

*TEMPERATURE DEPENDENCE OF COPPER RESISTIVITY INCLUDED IN CALCULATION OF POWER DENSITY

Figure 5. Power density profile for TE_{031} Simple Cavity Design No. 2.

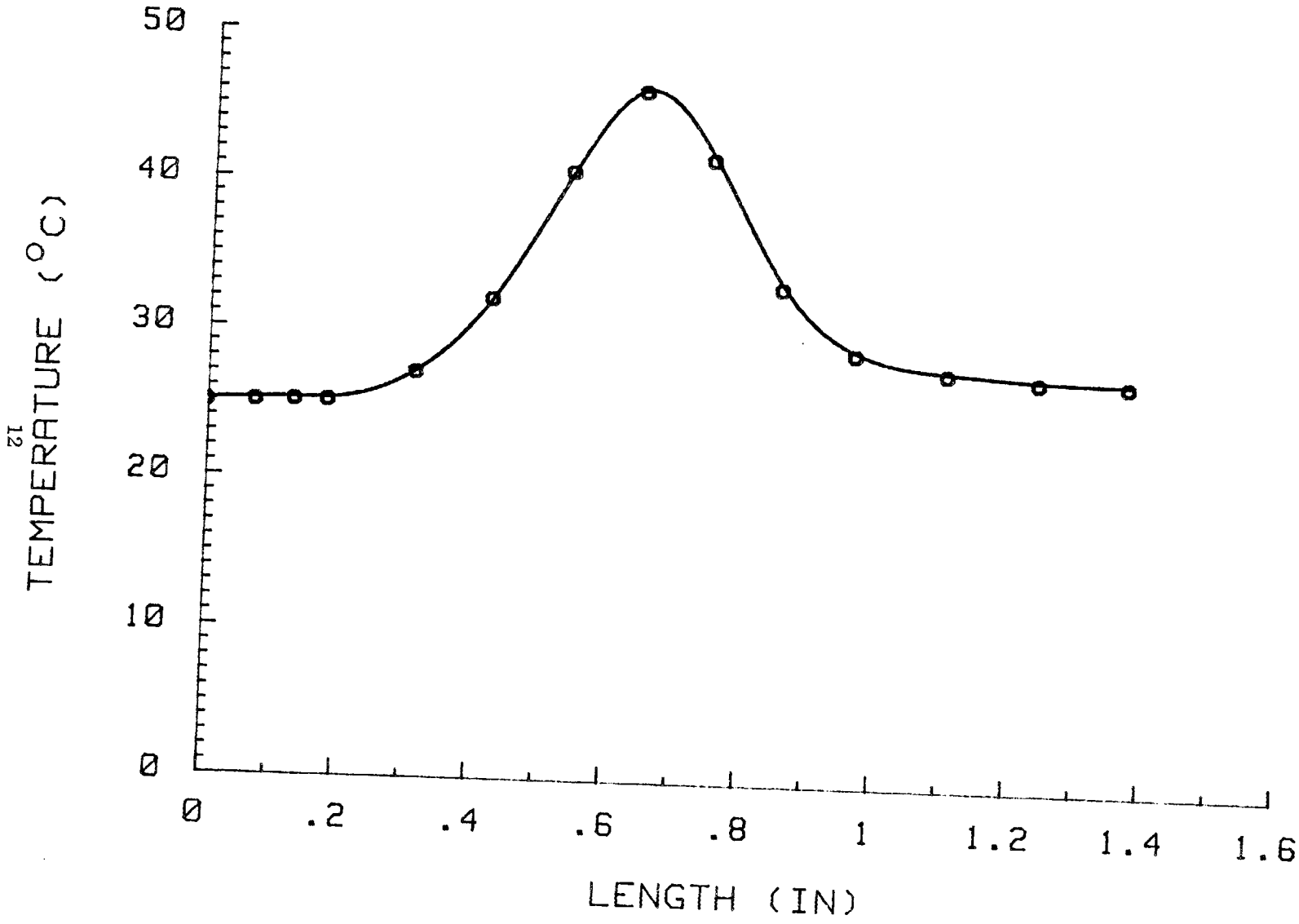

Figure 6. Temperature profile along inner wall of simple cavity for 10 kW CW output.

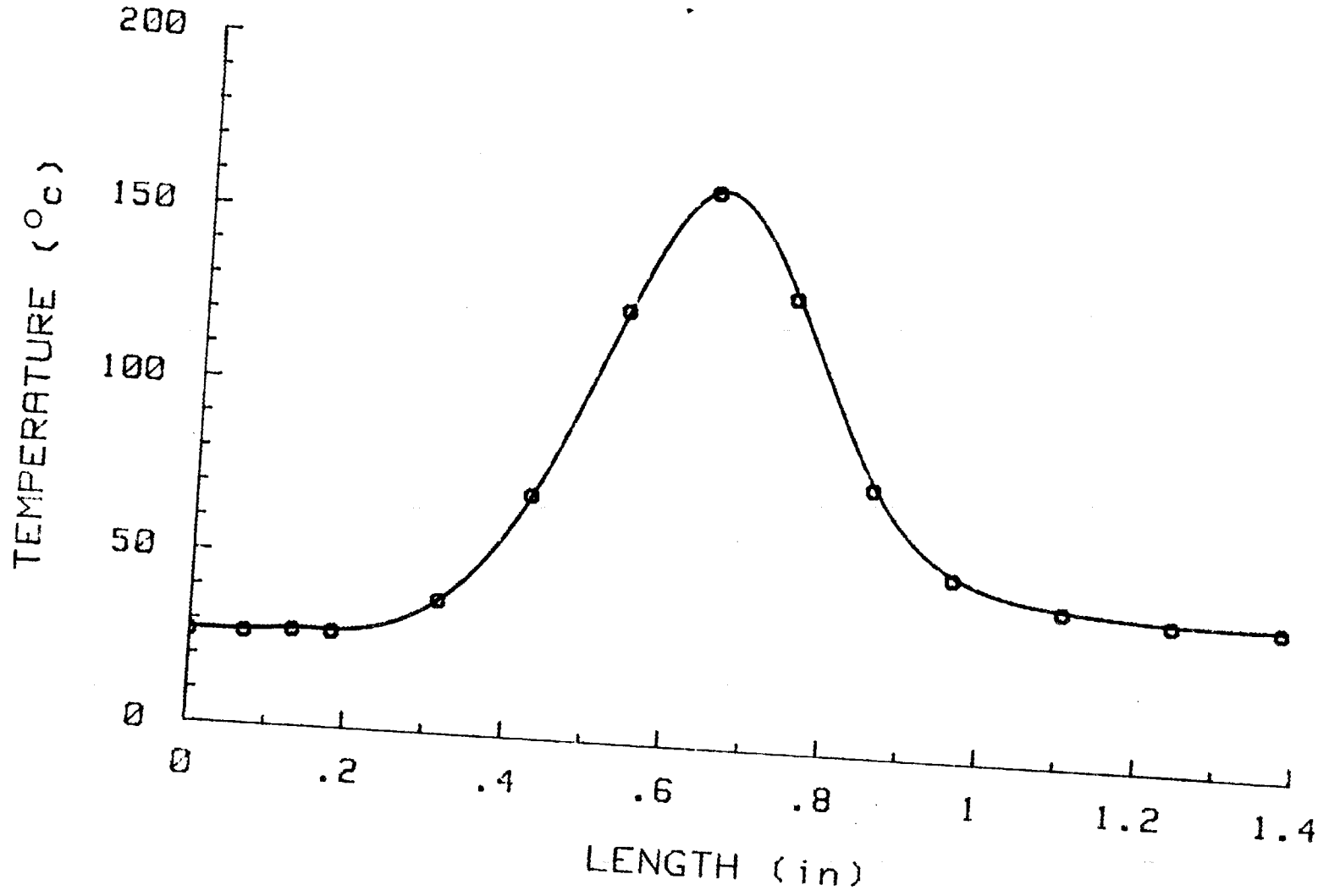

Figure 7. Temperature profile along inner wall of simple cavity for 50 kW CW output.

The temperature profile along the cooling channel (the hottest surface in contact with water) is given in Figure 8 for the 50 kW case. The 89°C peak temperature is well below the boiling point of water at typical operating pressure, and thus, should present no problems.

A second series of calculations were made to model the thermal effects of beam interception at the cavity entrance. 50 mA at 50 kV was assumed as a maximum interception, so 2.5 kW was input around the cavity entrance. The resulting temperature profile is shown in Figure 9. The peak temperature of 481°C is undesirably high, but at short intervals would probably not damage the cavity. Hopefully, the magnet steering coils can maintain beam interception at the cavity to well below 20 mA.

In summary, simple-cavity temperatures, under normal operation up to 50 kW CW, are quite safe. The associated thermal stresses and displacements are quite small, but are discussed in the complex cavity section of this report. Beam interception should be kept well below 2.5 kW for any appreciable operating period. Finally, corrosion and erosion should not be problems in the first tube because of the relatively low coolant velocities and brief test time.

Complex Cavity Design

The complex TE_{021}/TE_{031} cavity will be used in the second experimental tube, Preprototype Tube 1. The power density profile for a complex cavity operating at 100 kW CW output is shown in Figure 10. The parameters used in the thermomechanical calculations are as follows:

Material	OFHC Copper or AL-15 Copper
Tube Output Power	100 kW
Peak Power Density	5.75 kW/cm^2 or 6.33 kW/cm^2
Material Yield Strength	6.5 kpsi or 47 kpsi
Cooling Fluid	Oxygen-free Deionized Water
Coolant Velocity	60 ft/sec
Coolant Inlet Pressure	300 psi
Reynold's Number	22,600

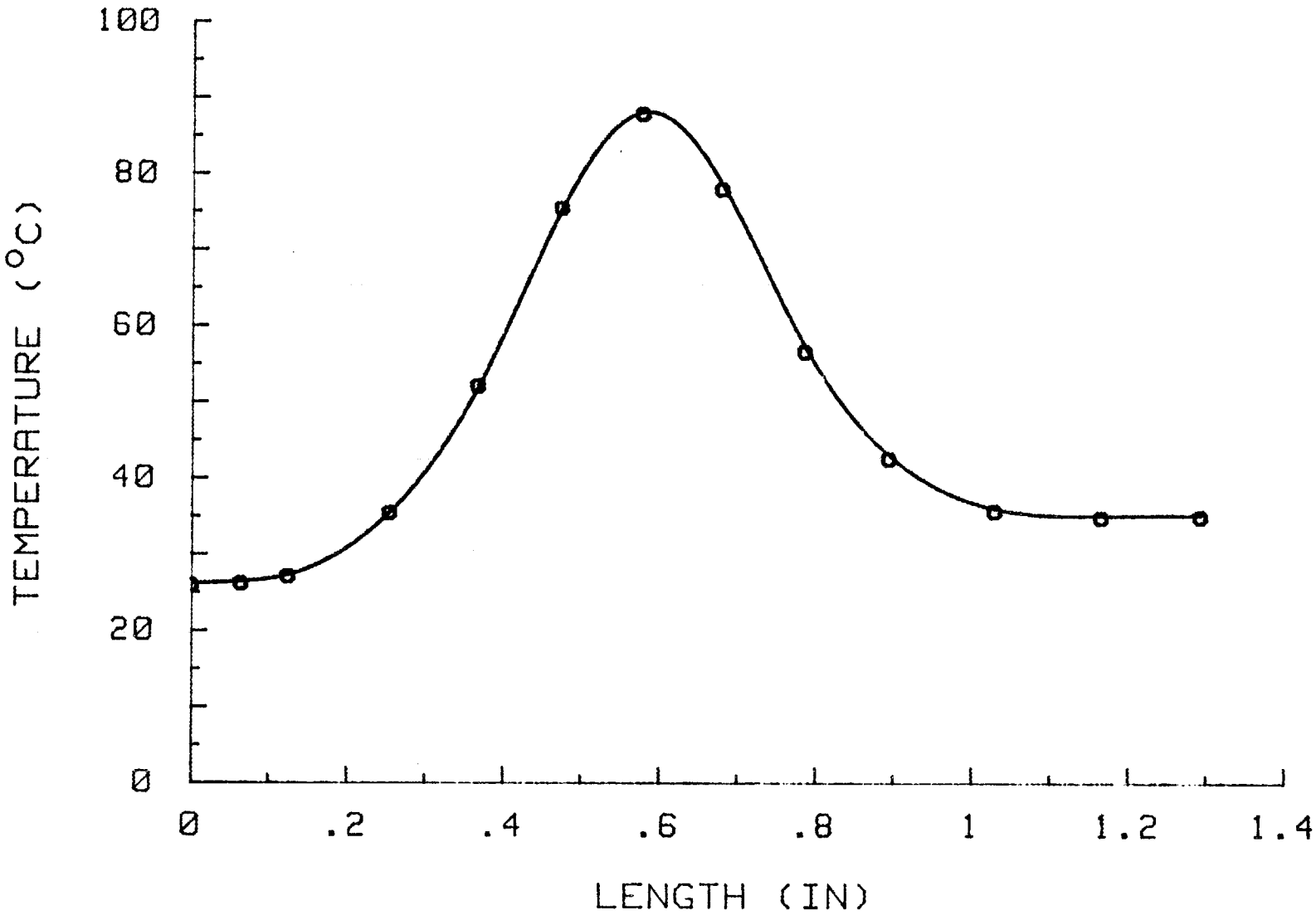

Figure 8. Temperature profile along cooling channel surface of simple cavity for 50 kW CW output.

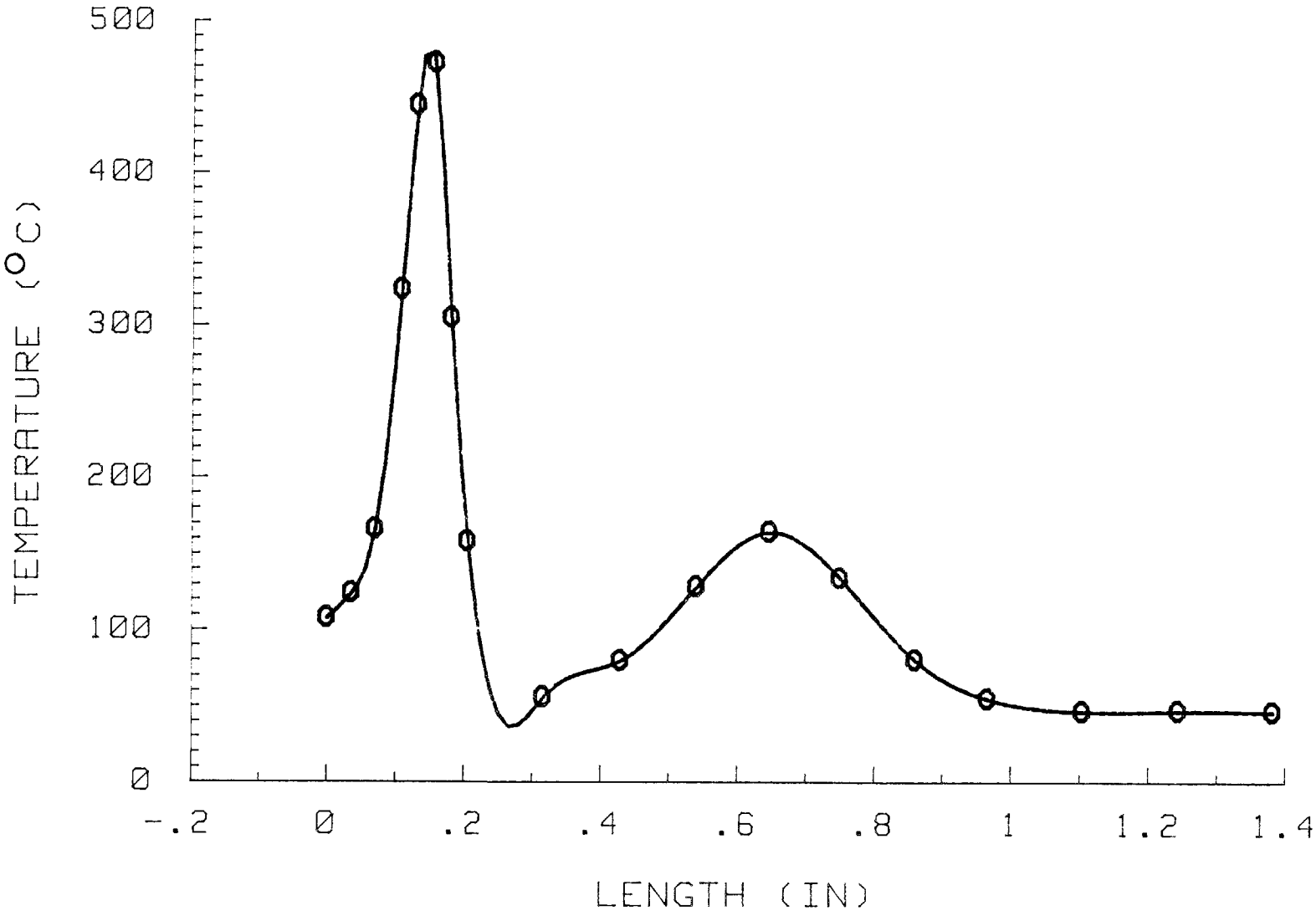

Figure 9. Temperature profile along cavity inner wall of simple cavity for 50 kW CW and 2.5 kW beam interception. (50 mA x 50 kV = 2.5 kW beam interception at cavity entrance)

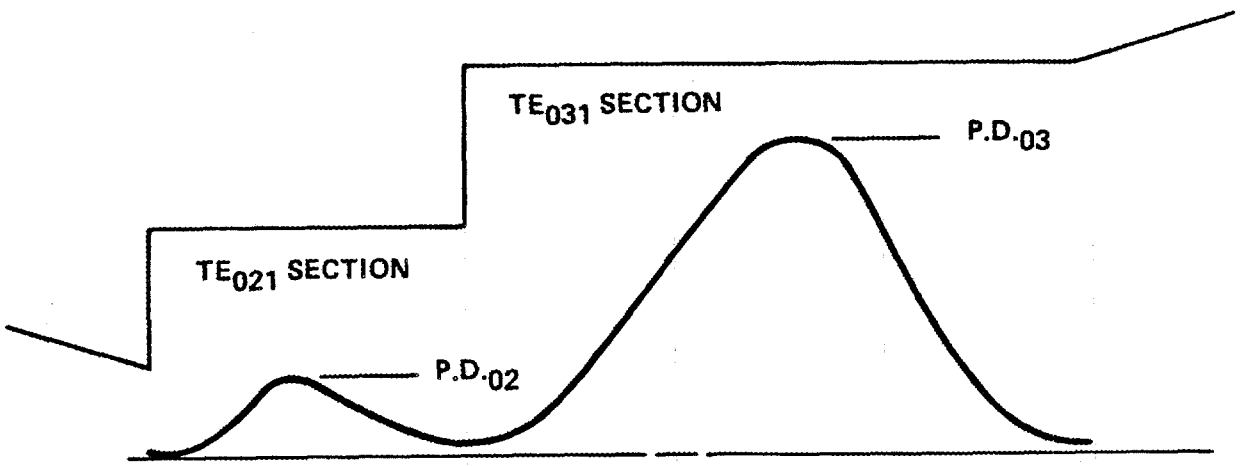

TYPE OF COPPER	OFHC	AL-15
$P.D._{02}\left(\frac{KW}{cm^2}\right)$	0.83	0.91
$P.D._{03}\left(\frac{KW}{cm^2}\right)$	5.75	6.33

Figure 10. Power density profile for TE_{021}/TE_{031} complex cavity for 100 KW CW operation.

It is important to note that these calculations allow for the plastic deformation that occurs when a ductile material is stressed beyond its yield strength. Because the yield strengths of OFHC and AL-15 coppers are so different, the two materials are directly compared in the following calculations.

Temperatures along the cavity wall and cooling channel surface are given for OFHC in Figures 11 and 12, respectively, and for AL-15 in Figures 13 and 14. The small difference in temperature between the two materials is due to AL-15's slightly lower thermal and electrical conductivities. All of these temperature profiles are sufficiently low enough to avoid, both, damage to the copper and pool boiling in the water channels.

Figures 15 and 16 give the stress profiles along the cavity wall and cooling channel, respectively, for OFHC copper. The peak stress is naturally very close to the yield strength of the material. It can, however, be slightly higher than the yield strength because work hardening takes place in the material during yielding.

Figures 17 and 18 give similar profiles for AL-15 copper. Comparing the stress profiles for the two materials, the effects of the higher yield stress on the overall stress distribution are evident. It is difficult to interpret which material gives the preferred stress profile, since both materials are yielding. However, a fatigue failure calculation indicating how many complete cycles the cavity can withstand before failing will give a good indication of the preferred material. There may also be manufacturing considerations that complicate the use of AL-15; these are currently being investigated.

Figures 19 and 20 show the actual deformation of the cavity inner wall for OFHC and AL-15. These deformations result from the combined effects of thermal expansion and yielding. The maximum displacement in the OFHC cavity is about a third of a mil, extending towards the cavity centerline. The displacement of the AL-15 cavity is entirely away from the cavity

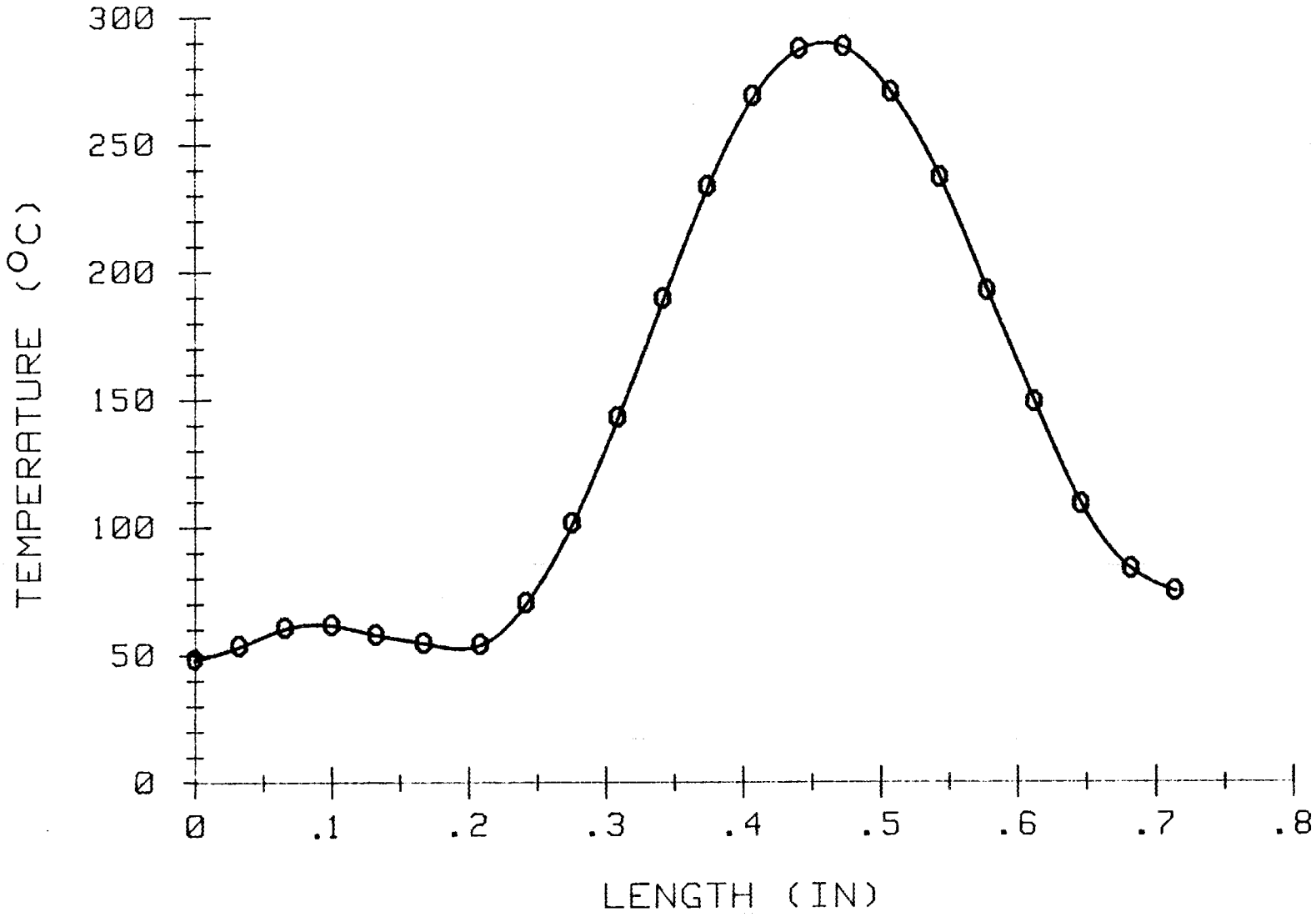

Figure 11. Temperature profile along the inner wall of the complex cavity made from OFHC copper.

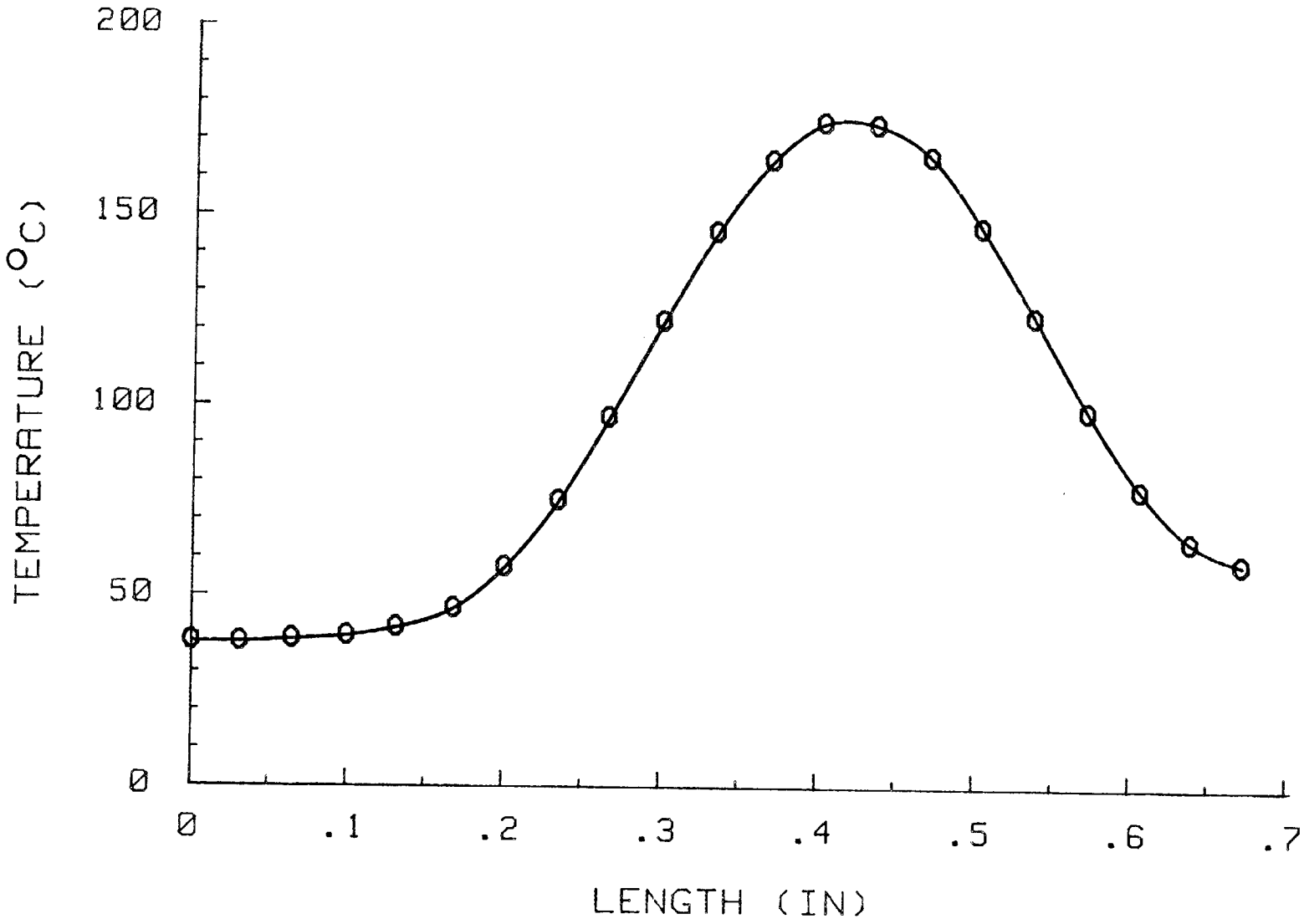

Figure 12. Temperature profile along cooling channel surface of complex cavity made from OFHC copper.

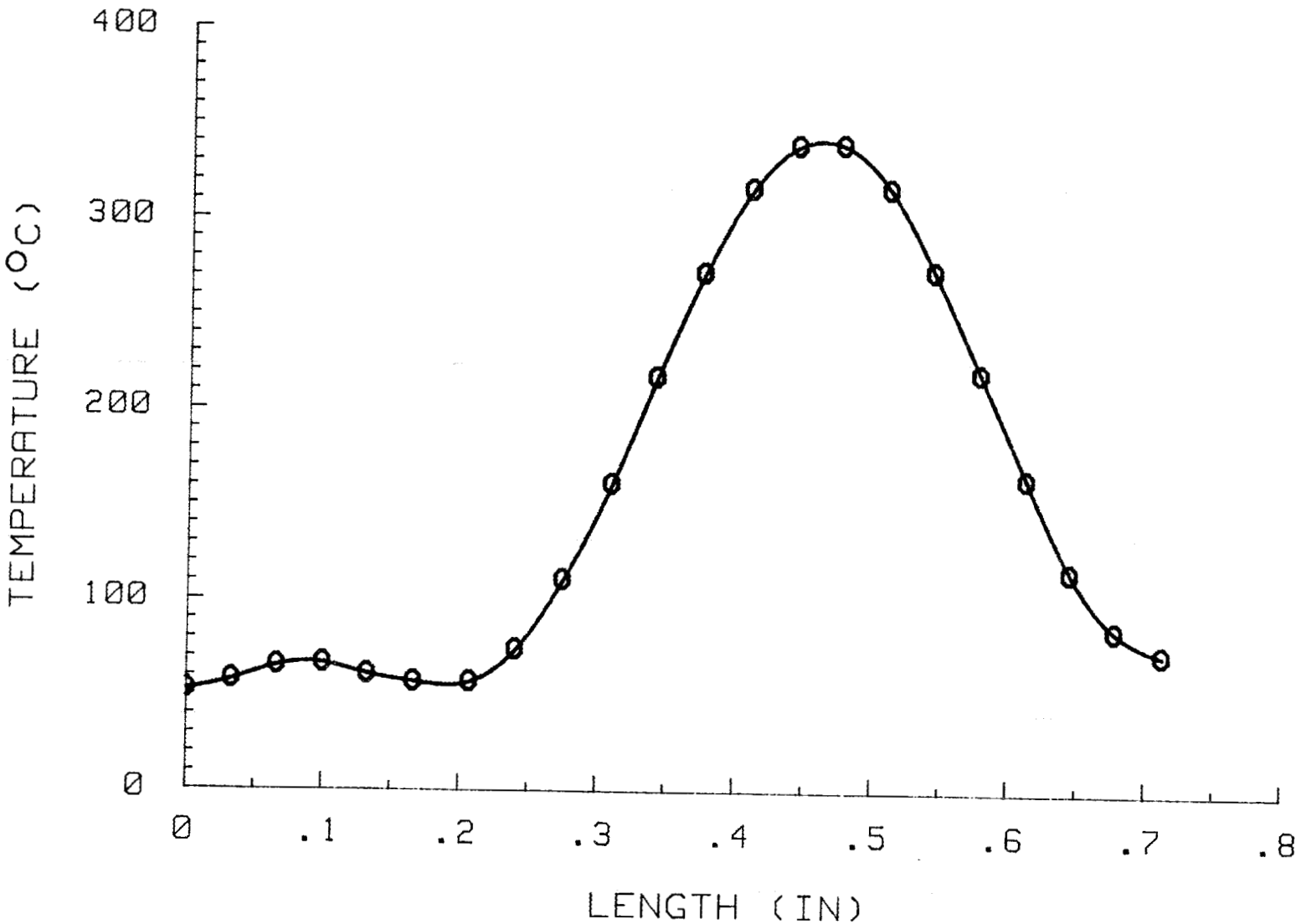

Figure 13. Temperature profile along inner wall of complex cavity made from AL-15 copper.

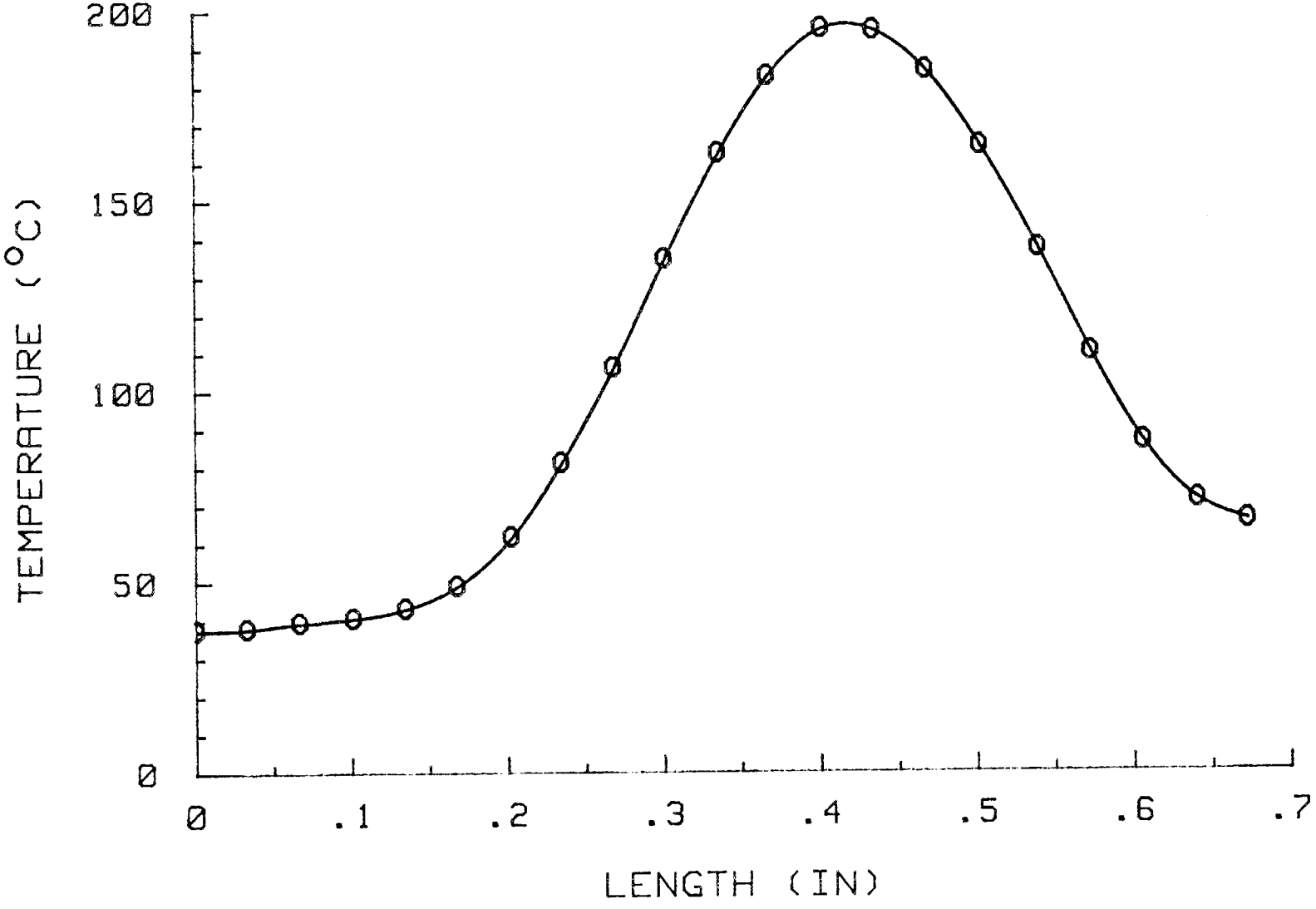

Figure 14. Temperature profile along cooling channel surface of complex cavity made from AL-15 copper.

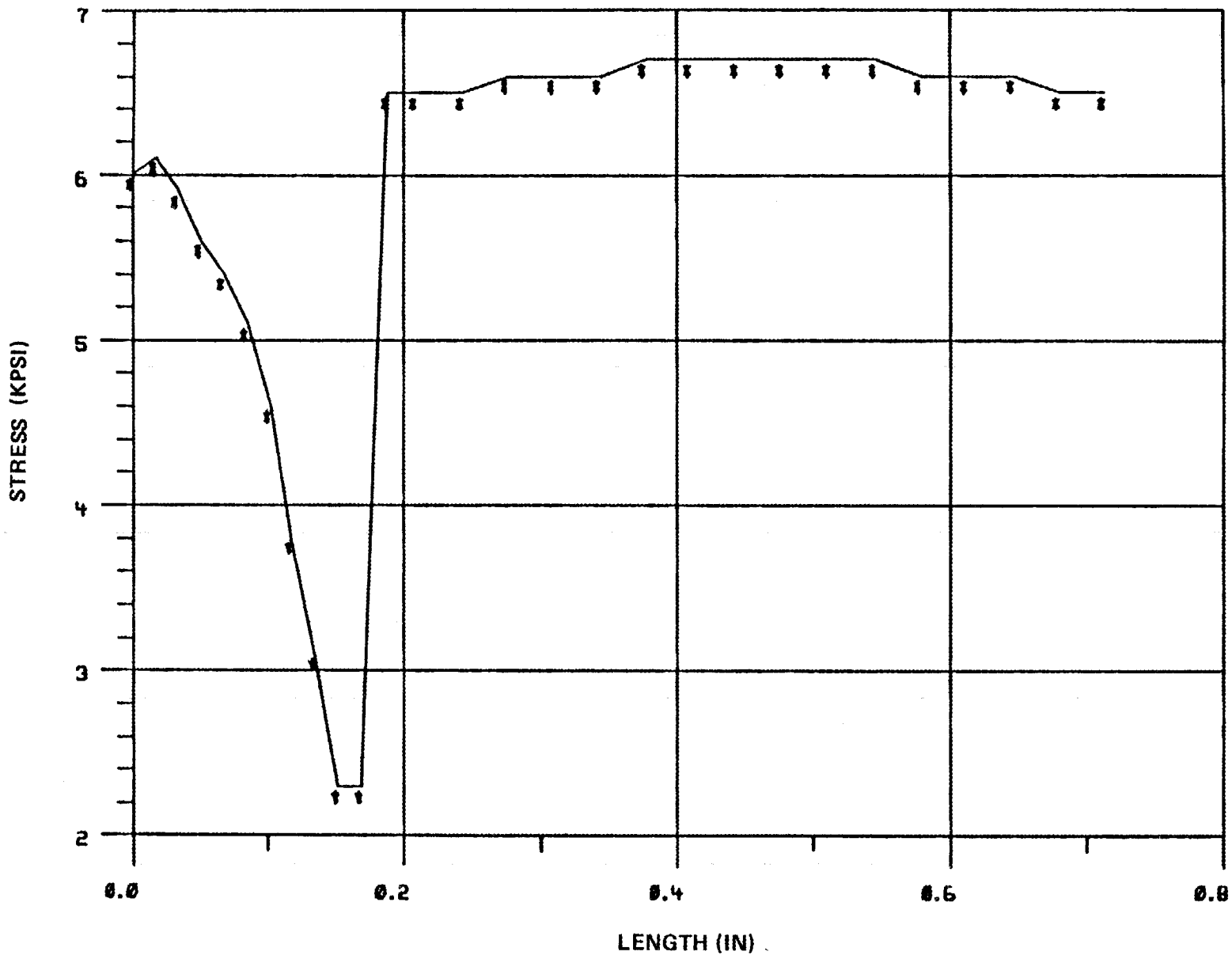

Figure 15. Stress profile along inner wall of complex cavity made from OFHC copper.

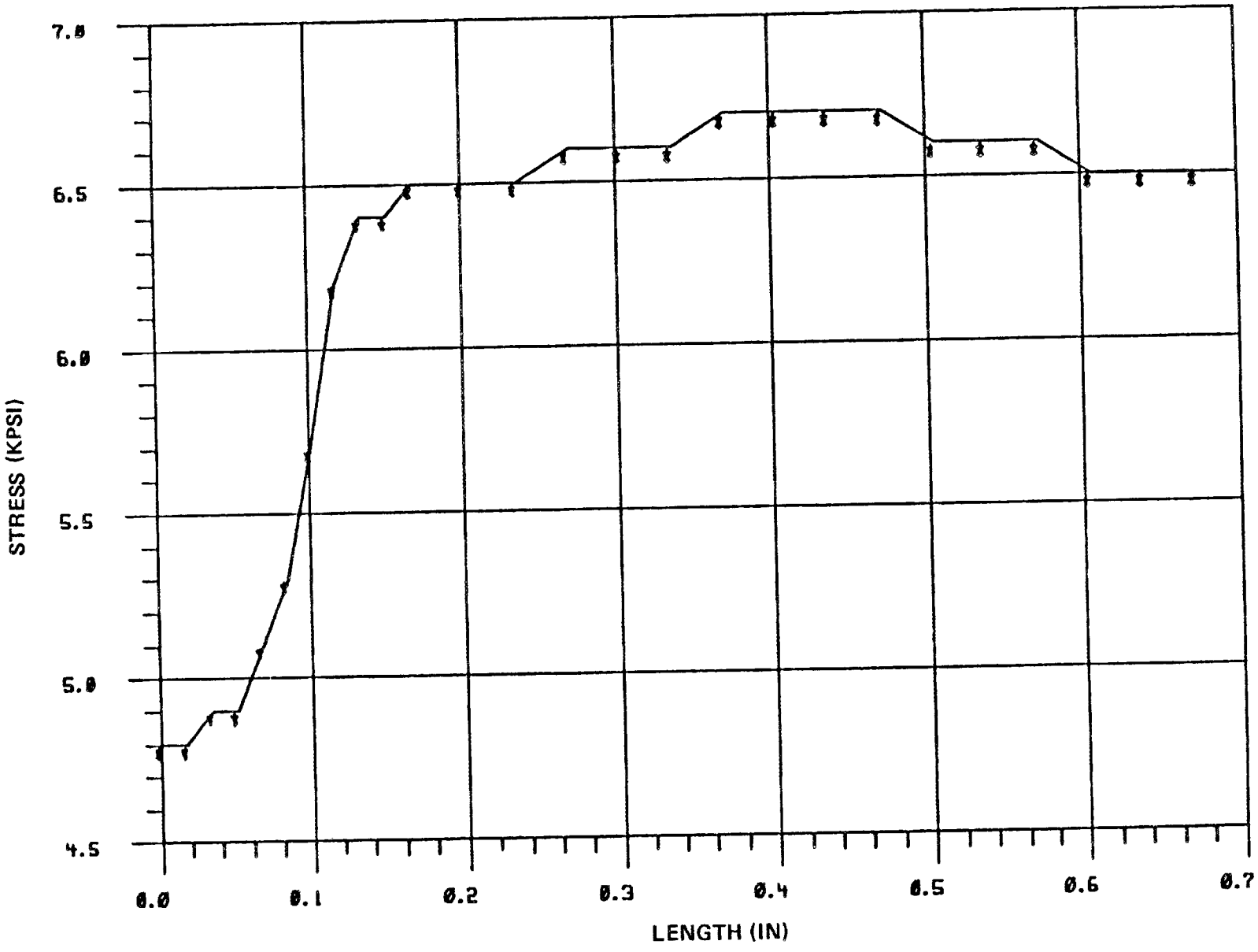

Figure 16. Stress profile along cooling cahnnel surface of complex cavity made from OFHC copper.

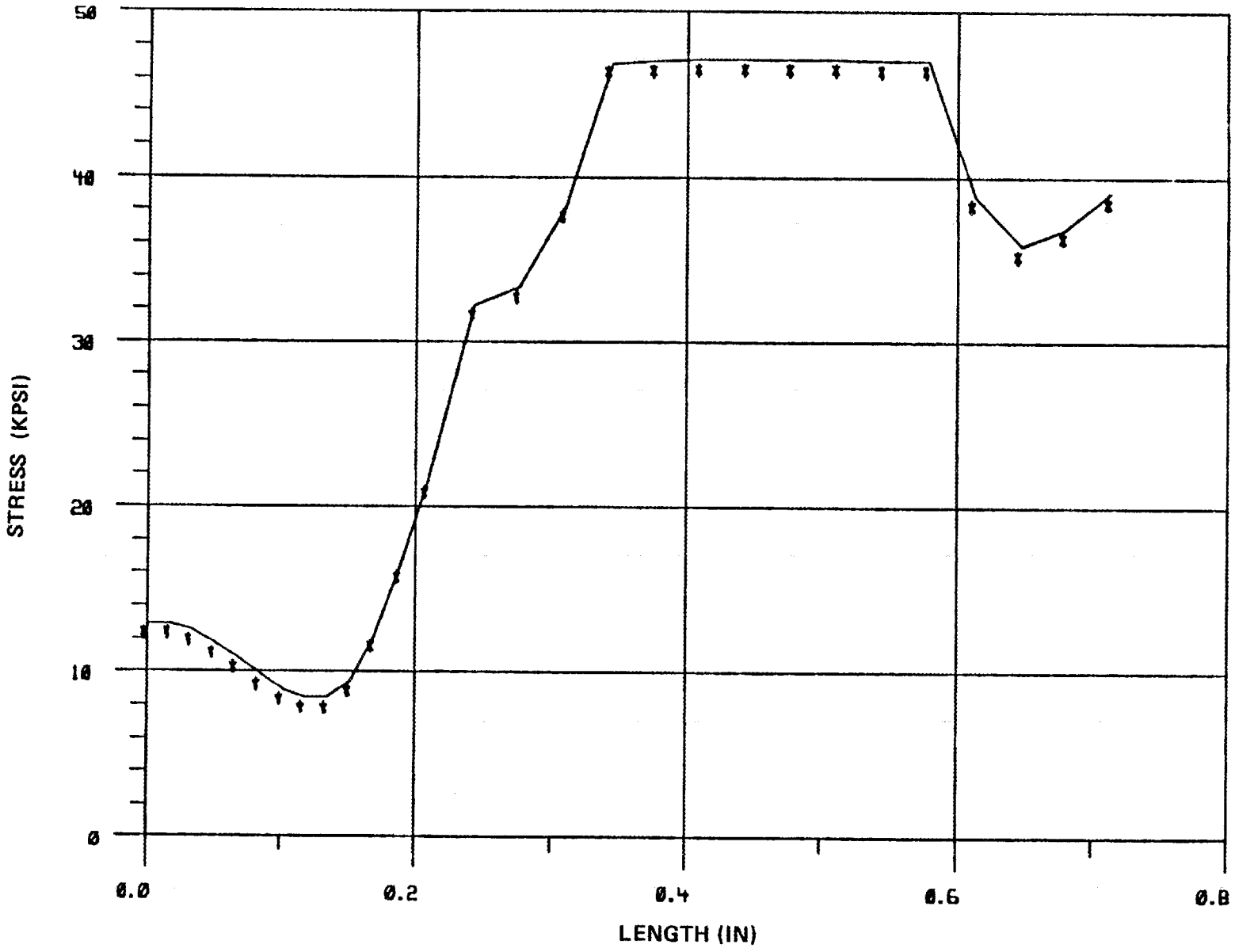

Figure 17. Stress profile along inner wall of complex cavity made from AL-15 copper

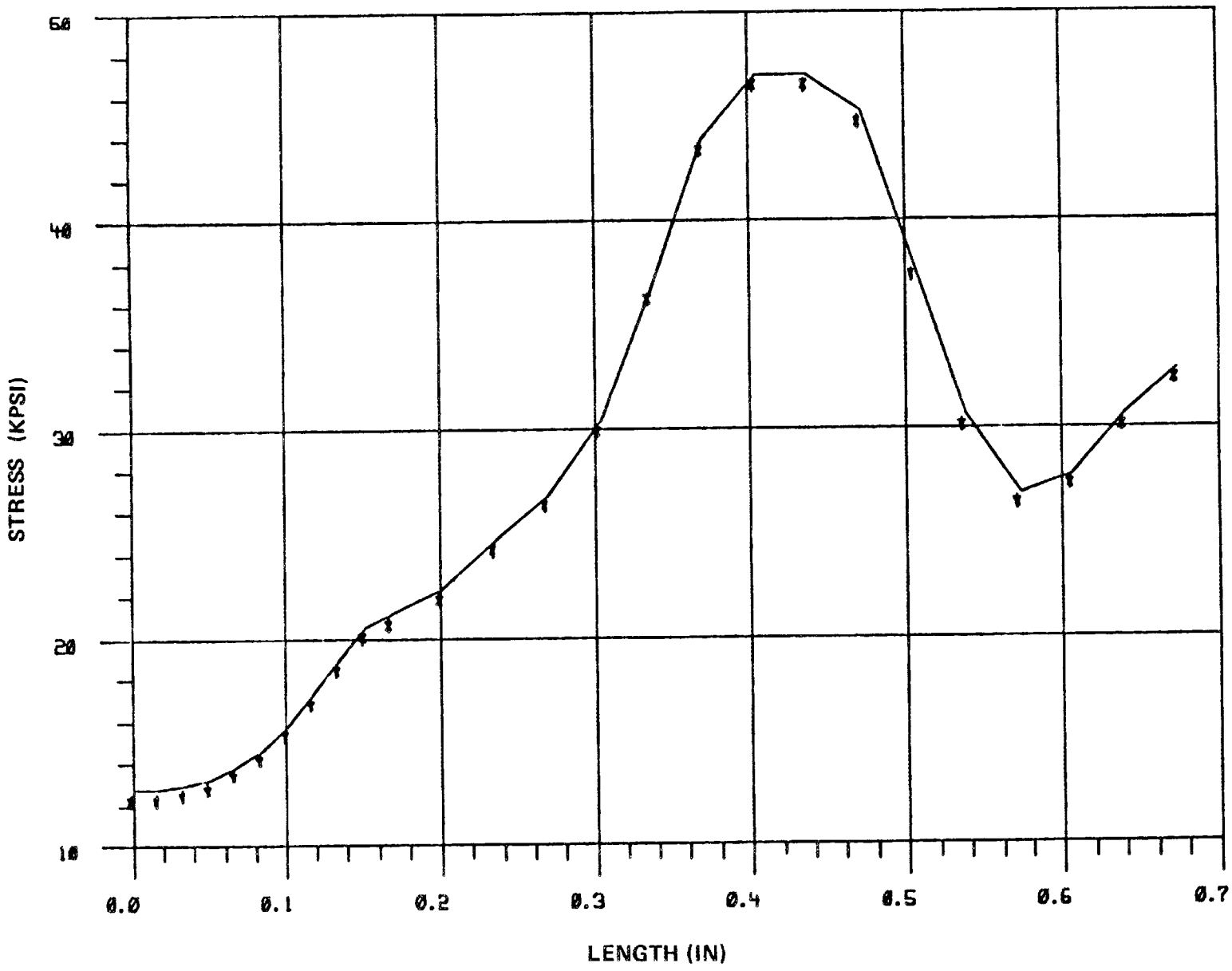

Figure 18. Stress profile along cooling channel surface of complex cavity made from AL-15 copper.

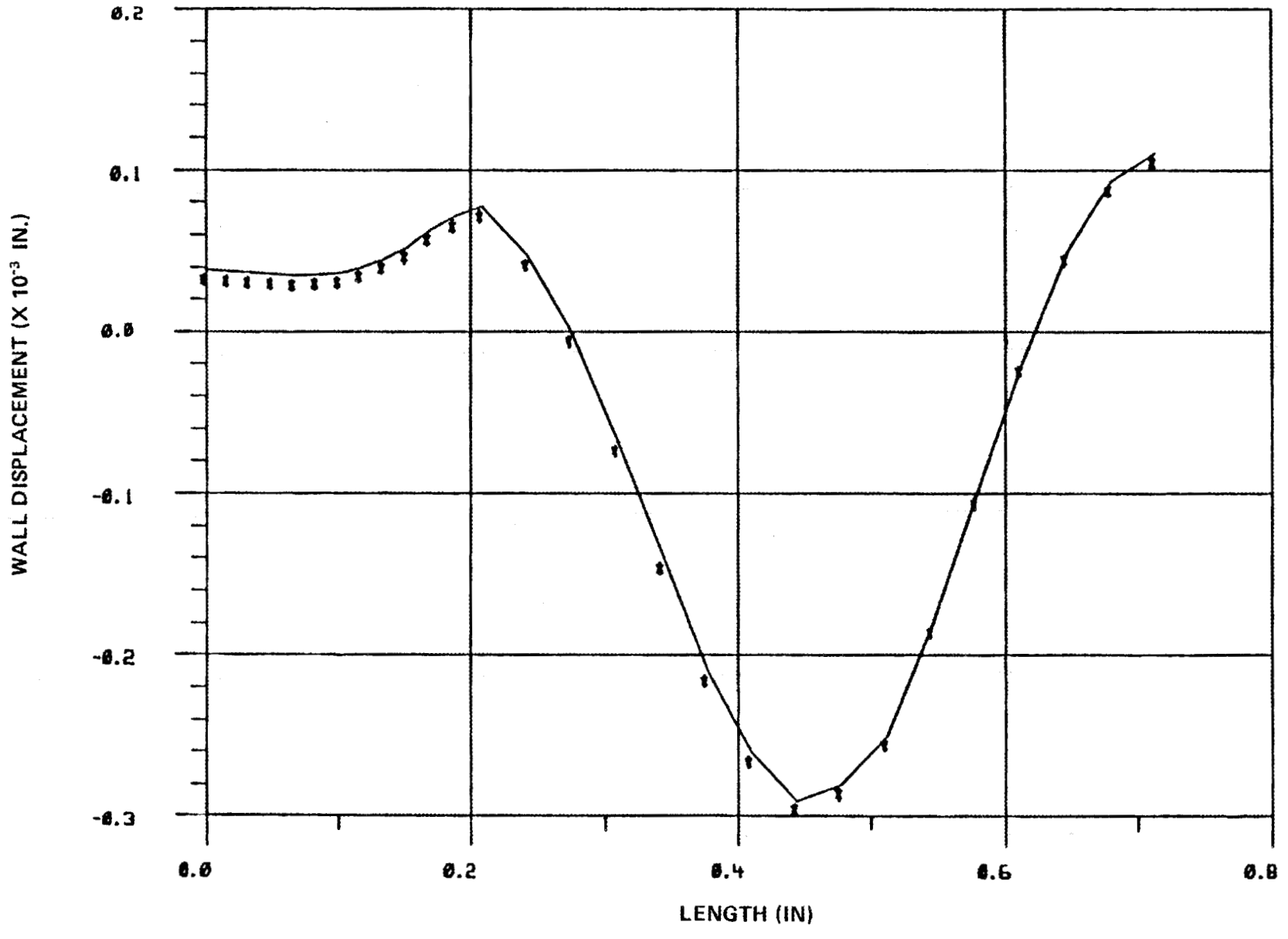

Figure 19. Displacement profile along the inner wall of complex cavity made from OFHC copper.

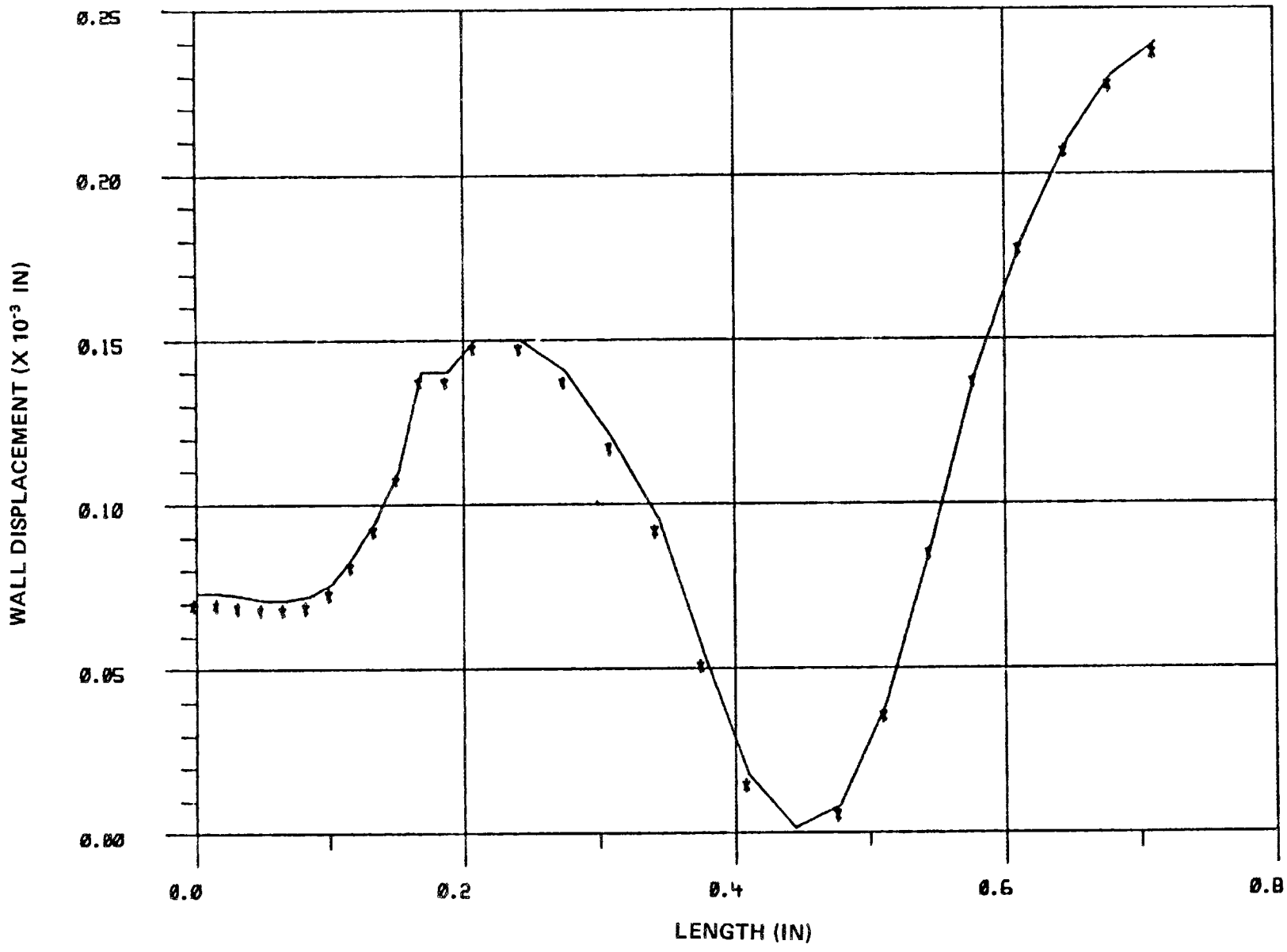

Figure 20. Displacement profile along the inner wall of the complex cavity made from AL-15 copper.

centerline, with a peak displacement of about a fourth of a mil. The relationship between the different properties of the two materials and the calculated cavity wall deformations is not yet understood. These deformations should not noticeably affect the electrical performance of the cavity. A sensitivity analysis will be performed to confirm this.

C. BEAM TUNNEL CONSIDERATIONS

The beam tunnel is the portion of the tube between the electron gun and the output cavity. In this region the electron beam is adiabatically compressed to the proper size for interaction in the cavity. The length of this region is determined by the dynamics of the electron beam and the constraints of the magnet design. The structure in this region must be large enough to allow for proper beam transmission, yet small enough to absorb the microwaves that leak out of the back of the cavity. If too much power leaks back to the gun, beam and cathode instabilities can occur which could affect tube performance. In addition to absorbing back-rf leakage and avoiding beam interception, the beam tunnel must also be shaped to prevent the electron beam from interacting with any resonant modes of the beam tunnel. Therefore, a good beam tunnel design must achieve a balanced tradeoff between these often conflicting requirements.

To provide for proper beam clearance, a maximum filling factor is chosen based on previous experience and the ability of the magnet manufacturer to build a straight magnet. The criteria used is that the diameter of the beam be less than 80% of the diameter of the beam tunnel. We have had to violate this criteria in the 140 GHz design. In the area immediately prior to the output cavity, it is necessary to cut-off the TE_{02} mode. The filling factor in this area is close to 90%. To provide beam transmission through this area, we have installed trim coils in the magnet to steer the beam. A minimum diameter for the rest of the beam tunnel is determined by the maximum filling factor coupled with information on the electron beam size and the magnetic field.

Beam tunnel loss is provided by rings of a lossy ceramic material. To prevent charging of the ceramic by electron bombardment, the lossy rings are

alternated with smaller diameter copper rings. The heater of the electron gun requires an input power of 28 watts to obtain 8 A of beam current. To provide 1% beam current stability in the tube, the rf heating must be limited to less than 280 mW. The back rf leakage from the cavity is calculated to be 1.5 kW (see Section III A). To adequately isolate the cathode, at least 37 dB of insertion loss is necessary to reduce the 1.5 kW of rf leakage to 280 mW. This estimate assumes that all rf power reaching the gun region is absorbed by the cathode which is a worst case scenario. The present design is being measured in the cold test laboratory to verify that it provides the required insertion loss.

Although we must provide enough loss in the beam tunnel design, we must not introduce too much. The ceramic rings closest to the cavity can absorb too much power and possibly become overheated and crack. Thermal calculations were performed this quarter to verify the performance of the first ceramic ring, assuming a value of one kilowatt of back-rf leakage from the cavity (a back-rf leakage of 1% while operating at 100 kW). In cold test measurements, the loss in the first ring was determined to be 25% of the back-rf power in cold test measurements.

A temperature and stress analysis of the first ceramic ring was conducted using the MARC analysis computer code. Two cases were analyzed; a worst case analysis where the ring absorbed the entire one kilowatt of rf leakage, and a more realistic case where the ring absorbed 25% of the power, or 250 watts. In each case the power is assumed to be equally distributed axially along the inner surface of the ring. For the worst case analysis, the temperature profile of the ring is given in Figure 21. The maximum temperature reached is 123°C along the inside edge of the ring. Figure 22 gives the hoop stress within the ring. A maximum tensile stress of 18 kpsi is reached. This is close to the 20 kpsi ultimate tensile strength of the material. The temperature profile for the 250 watts absorption case is given in Figure 23. The maximum temperature reached is 61°C, again along the inside edge of the ring. The hoop stress is given in Figure 24. The maximum tensile hoop stress is given in 8.4 kpsi. This level of stress is well below the ultimate tensile strength of the material.

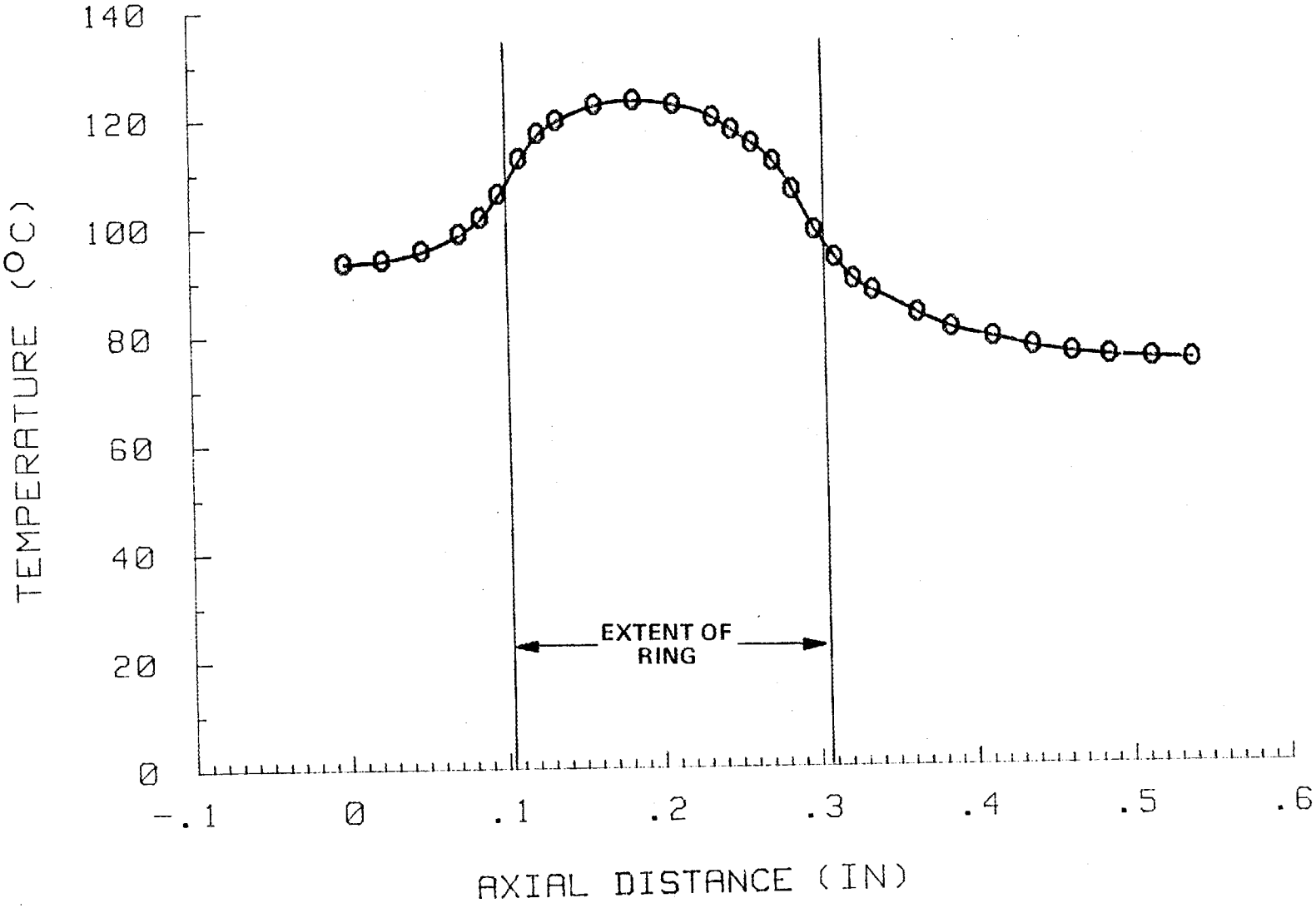

Figure 21. Axial temperature profile along beam tunnel I.D. for 1 kW absorbed power in first ceramic ring.

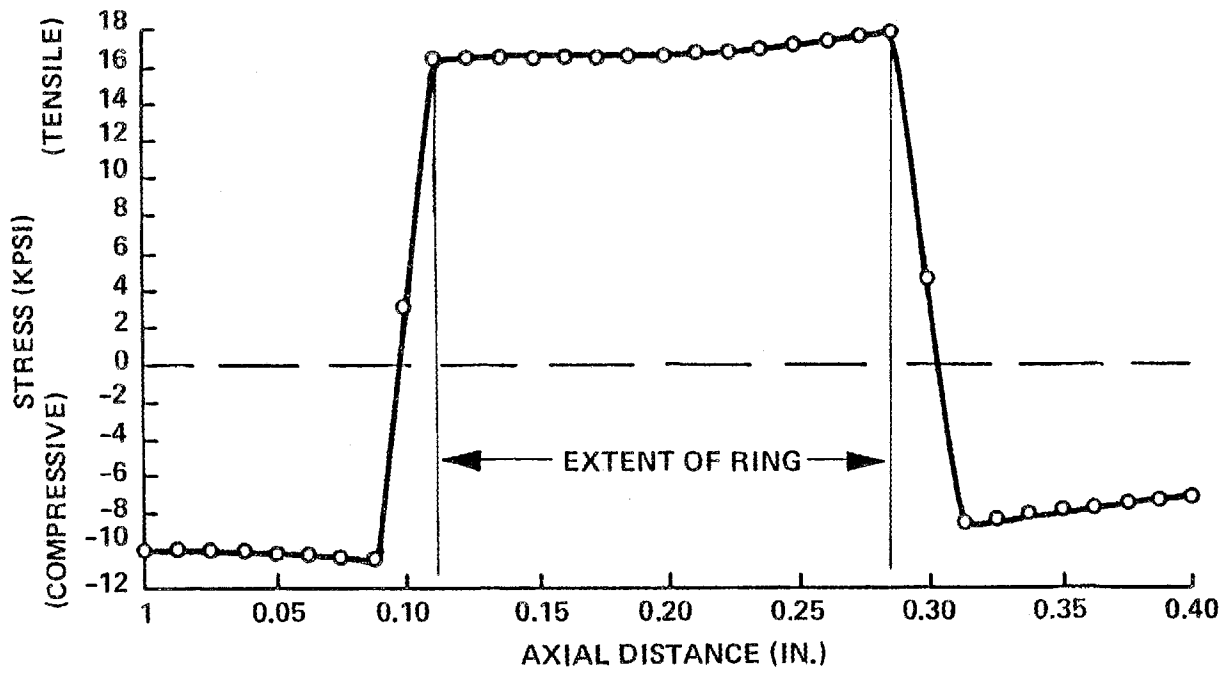

Figure 22. Axial hoop stress profile at the radius of maximum tensile stress for 1 kW absorbed power in first ceramic ring.

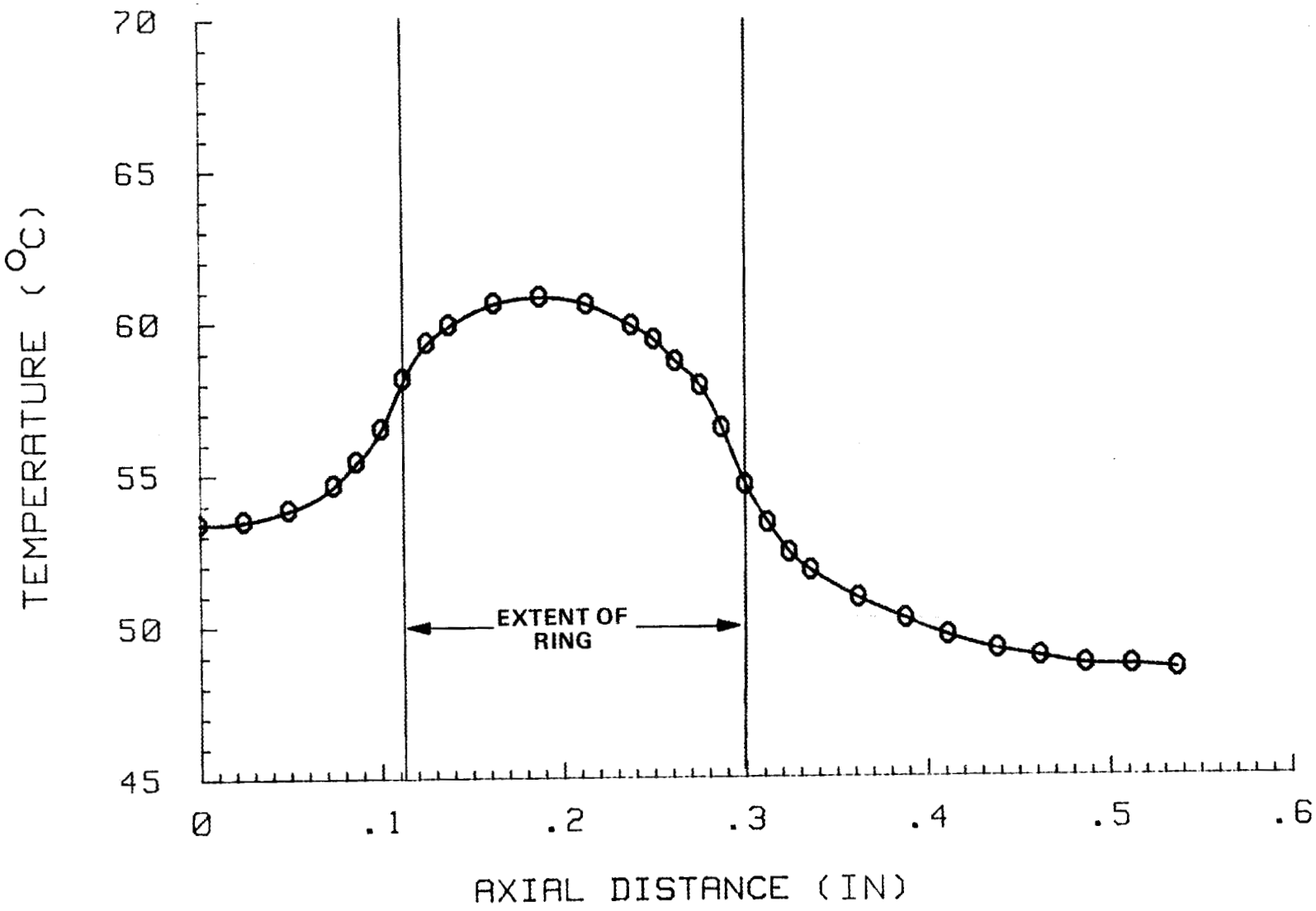

Figure 23. Axial temperature profile along beam tunnel I.D. for 250 W absorbed power in first ceramic ring.

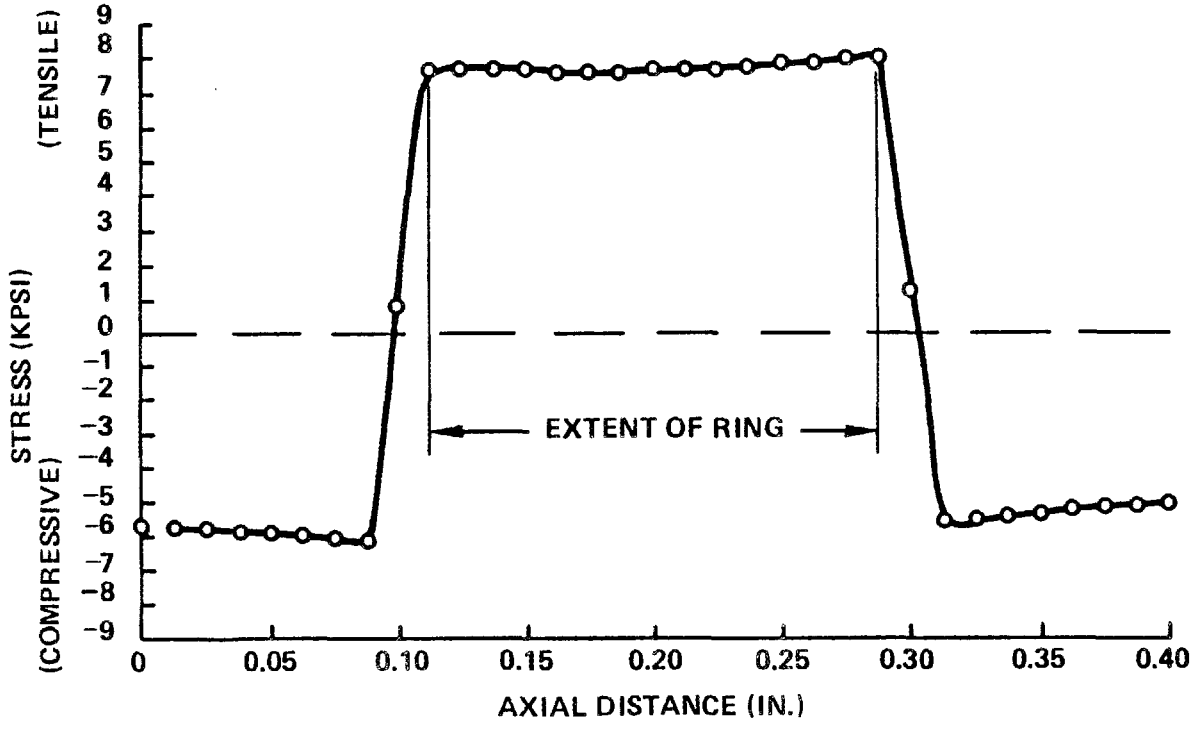

Figure 24. Axial hoop stress profile at the radius of maximum tensile stress for 250 W absorbed power in the first ceramic ring.

To summarize, the beam tunnel design must provide adequate clearance for beam transmission, but must also isolate the cathode from the back-rf leakage of the cavity. Our present design is being tested to verify that it provides adequate rf loss. Trim coils have been installed in the magnet system to steer the beam through the stringent clearance areas of the beam tunnel. In addition, a temperature and stress analysis of the ceramic ring closest the the cavity was performed. The analysis indicates that we are well within the limits of the material with this design. The power absorbtion capacity of the first ring is about one kilowatt, which is a factor of four higher than the normal operating condition.

IV. COLLECTOR

A. OUTPUT TAPER DESIGN

Characteristics of the output taper design for Tube 1 have been discussed previously.[1] A tentative design for the high-mode purity taper for the second experimental tube has been completed. The mode content of this design at 140 GHz, assuming 100% TE_{03} mode at the cavity exit, is: 98.3%, TE_{03}; 0.0%, TE_{01}; 0.9%, TE_{02}; 0.1%, TE_{04}; 0.6%, TE_{05}; and less than 0.1% in higher order modes. For cavity operation at 137.2 GHz with 100%, TE_{23} mode at the cavity exit, the resultant mode purity is: 97.3%, TE_{23}; 0.1%, TE_{21}; 0.4%, TE_{22}; 0.5%, TE_{24}; 0.3%, TE_{25}; 0.1%, TM_{21}; 0.9%, TM_{22}; 0.3%, TM_{23}; and less than 0.1% in higher order modes. The total length of the output taper is 115.5 cm. Since the raised cosine taper achieves a 2.25-inch diameter quite rapidly, the effective collector area is similar to that using the simple linear taper of Experimental Tube 1. This taper design is currently being incorporated into the overall tube design.

V. OUTPUT WINDOW DESIGN

A. DOUBLE-DISC WINDOW

In this quarter, a fully three-dimensional, finite-element model of the proposed double-disc window was created and used to calculate the temperatures and stresses in the window. These calculations include the azimuthal variations in pressure and heat transfer coefficient. Previous three-dimensional results were inaccurate because the mesh used was not fine enough to give adequate resolution.[1] Thus, the first task was to validate our 3-D models.

To this end, we prepared three different finite-element models based on different element types. The first model, shown in Figure 25, is a simple two-dimensional model incorporating standard rectangular (flat brick) elements. The second model, shown in Figure 26, is a 3-D model using rectangular brick elements. In essence it is the same as the 2-D model, except that the addition of the third dimension prevents using as many mesh difference between shell and brick not clear divisions as in the 2-D model. The third model, shown in Figure 27, is made up of "shell" elements. Shell elements look similar to the bricks but they have the important difference that they can deform by bending as a result of the calculated stresses, whereas the bricks move only in translation. This important difference implies that only one layer of shell elements is necessary to represent the window thickness. Thus, we have reduced the number of elements by a factor of three, and can then add elements to subdivide the window more finely in the radial and azimuthal planes. This gives the necessary resolution for accurate calculations.

The same load was applied to all three models: a radially-varying pressure load typical of what the window must withstand during normal operation. Of course, the load was axisymmetric so that the 2-D case could be properly compared. The calculated window deflection for the 2-D control case is shown in Figure 28. The deflection at the window center is 0.00073 inches; at the edge it is 0.0019 inches. Figure 29 shows the results for the 3-D brick element model; they are clearly not in agreement with the

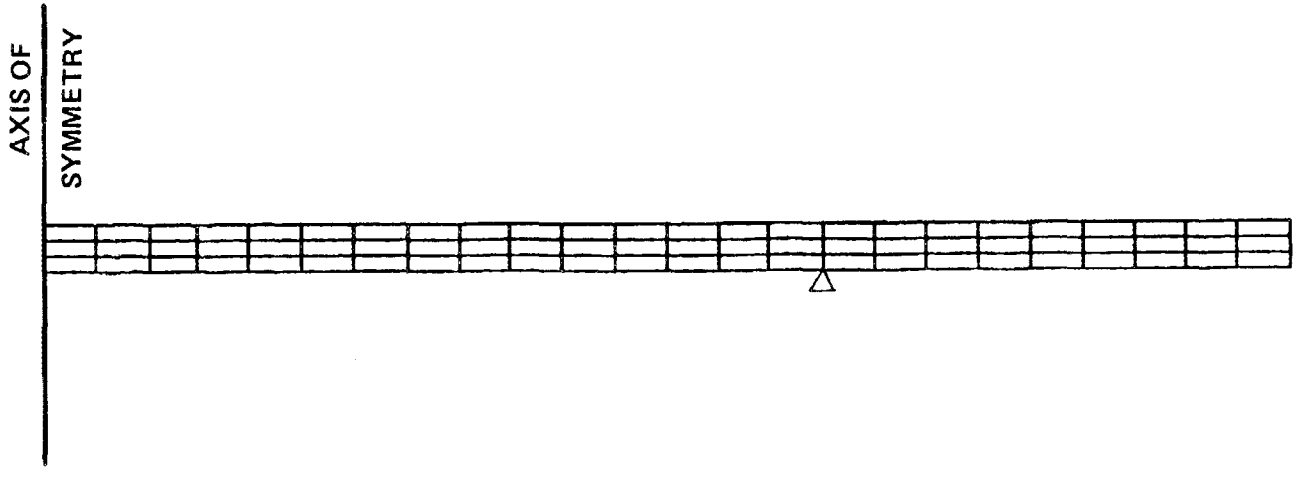

Figure 25. Validation of 3-D window structural model: Finite-element model for 2-D analysis.

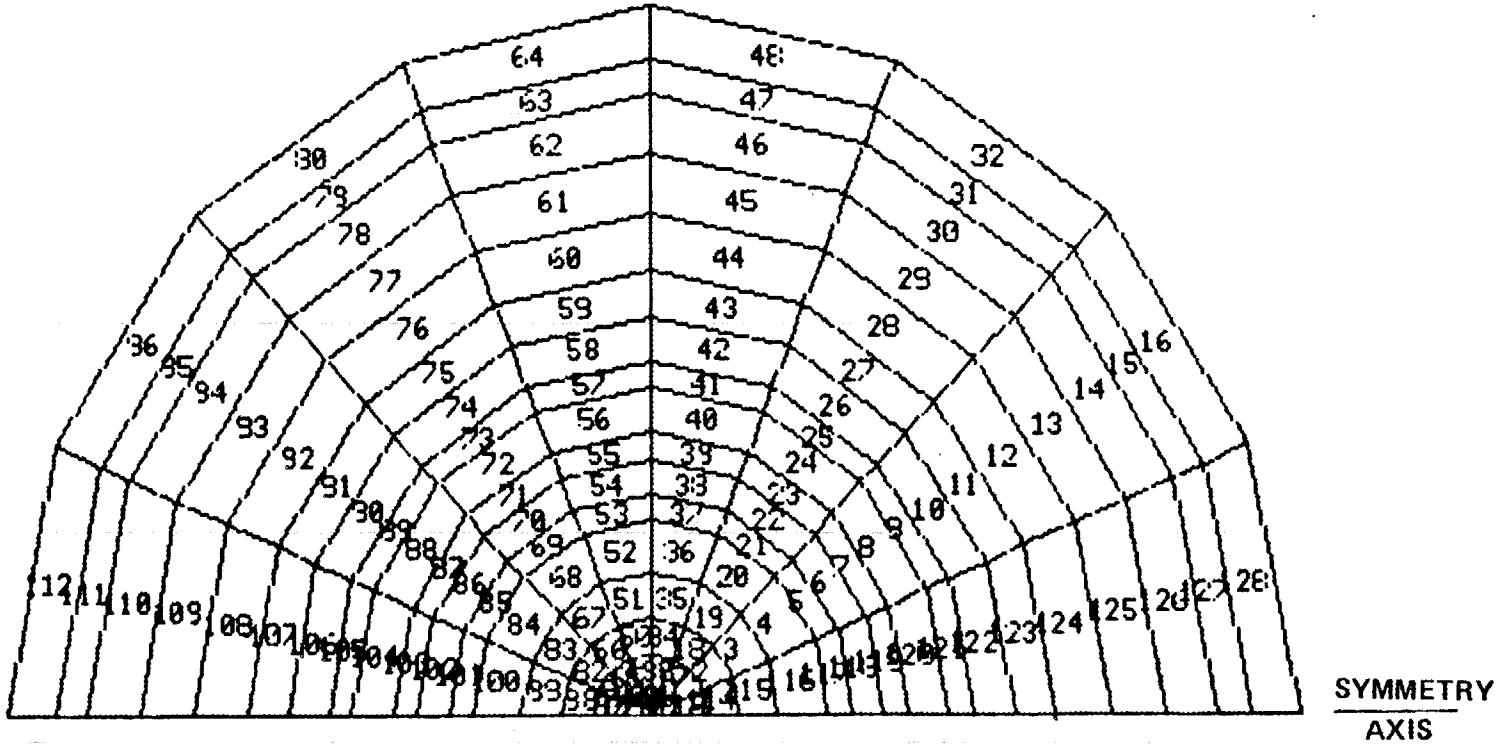

Figure 26. Validation of 3-D window structural model: Finite-element model for 3-D brick elements (3 elements across thickness).

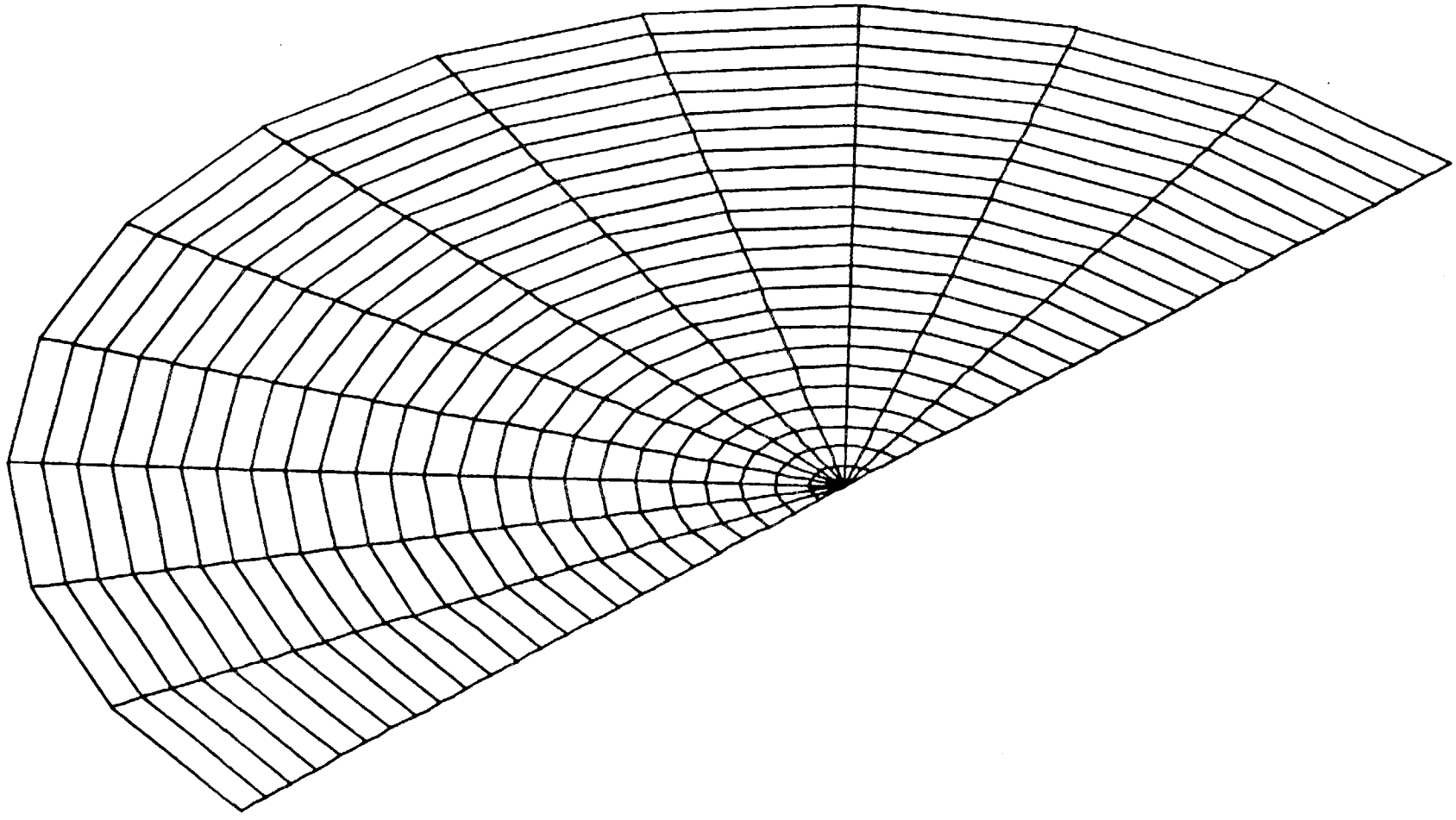

Figure 27. Validation of 3-D window structural model: Finite-element model for 3-D shell elements (2 element across thickness).

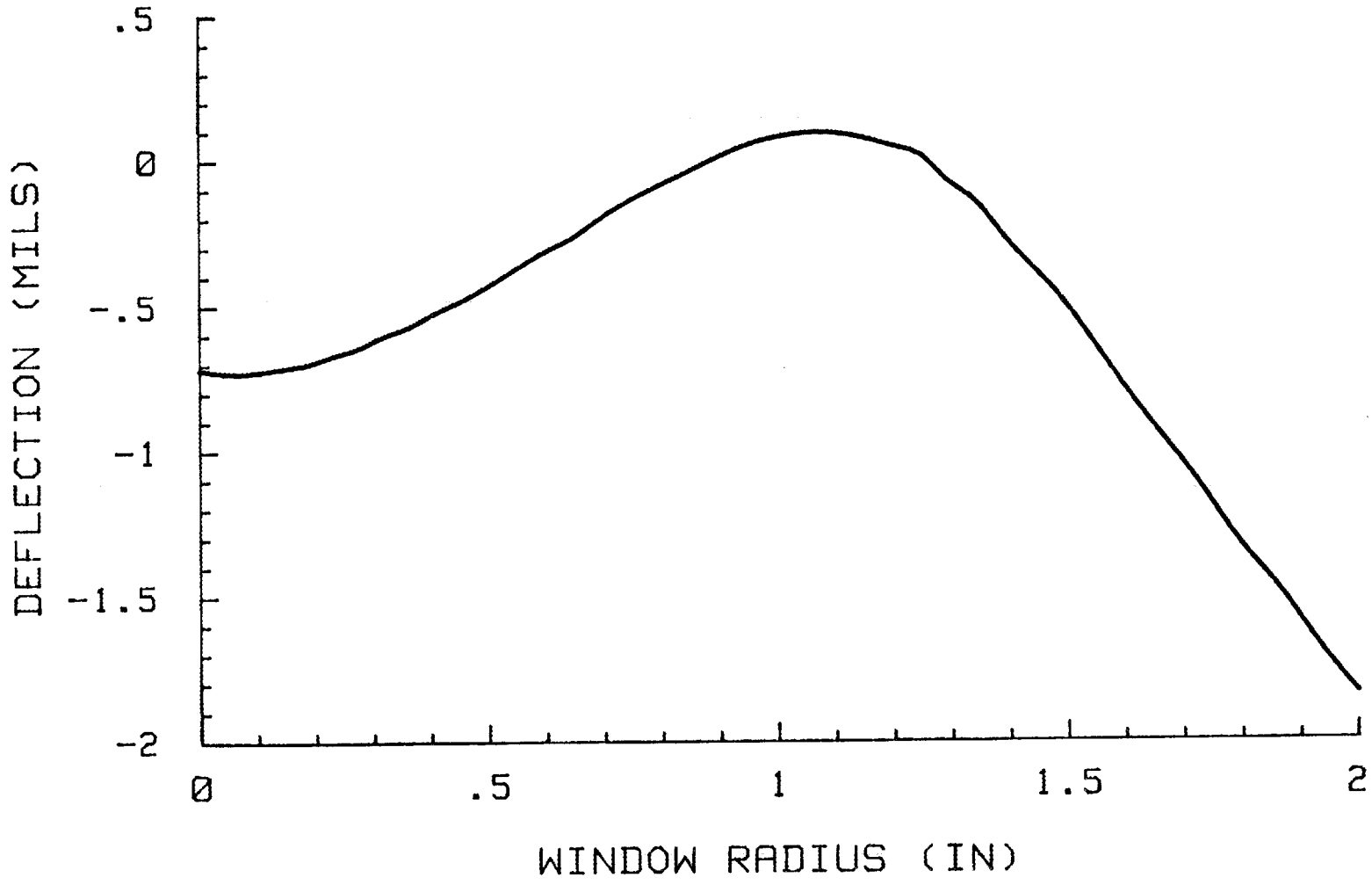

Figure 28. Validation of 3-D window structural model: Calculated window deflection for 2-D flat brick elements.

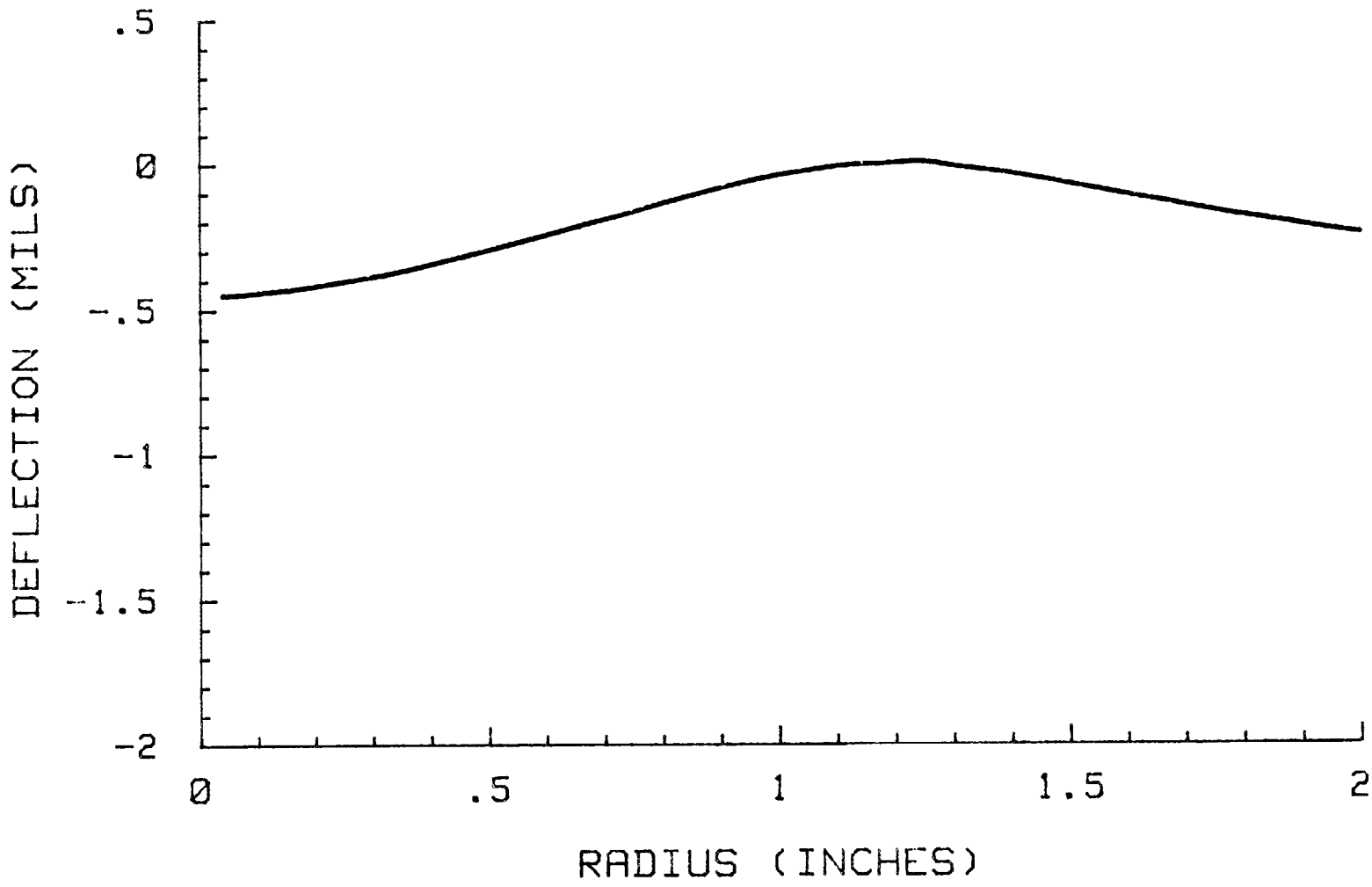

Figure 29. Validation of 3-D window structural model: Calculated window deflection for 3-D brick elements.

control case. Figure 30 shows the results for the 3-D shell element model; here the deflections agree with the control case to within 2%. Thus, we have good confidence that the non-axisymmetric results using this model will be representative of the actual stress and deflection values to within the uncertainty of the input data.

The actual window analysis was performed in three steps. First the stress due only to pressure load was calculated by estimating the pressure drop across the window and deriving a distributed load value. Next the absorbed microwave power for the TE_{03} mode was calculated and input with the variable heat transfer coefficient to give the temperature distributions. Finally the temperature results are input to a stress model to give the combined thermal and pressure stresses.

Relevant parameters are as follows:

Material	Sapphire
Loss Tangent	25 E-5[4]
Power	100 kW
Mode	TE_{03}
Disc Size	4" diameter
Cooling Fluid	FC-75 at 10°C
Coolant Flow Rate	31 GPM
Coolant Pressure	74 psi inlet; 25 psi outlet

Figure 31 is a schematic of the finite element model constructed to perform the thermal analysis. Figures 32 and 33 give the temperature distribution from the window center to the coolant inlet on the vacuum and FC-75 faces, respectively. The peak temperature on the vacuum side is 111°C, which is very close to the measured peak temperature of the 60 GHz, 200 kW window[5]. On the FC-75 side, the peak temperature is 82°C, which is well below the boiling point of FC-75, and so should not present any problem. The temperature profiles at other azimuthal locations (e.g. center-to-outlet) are very similar.

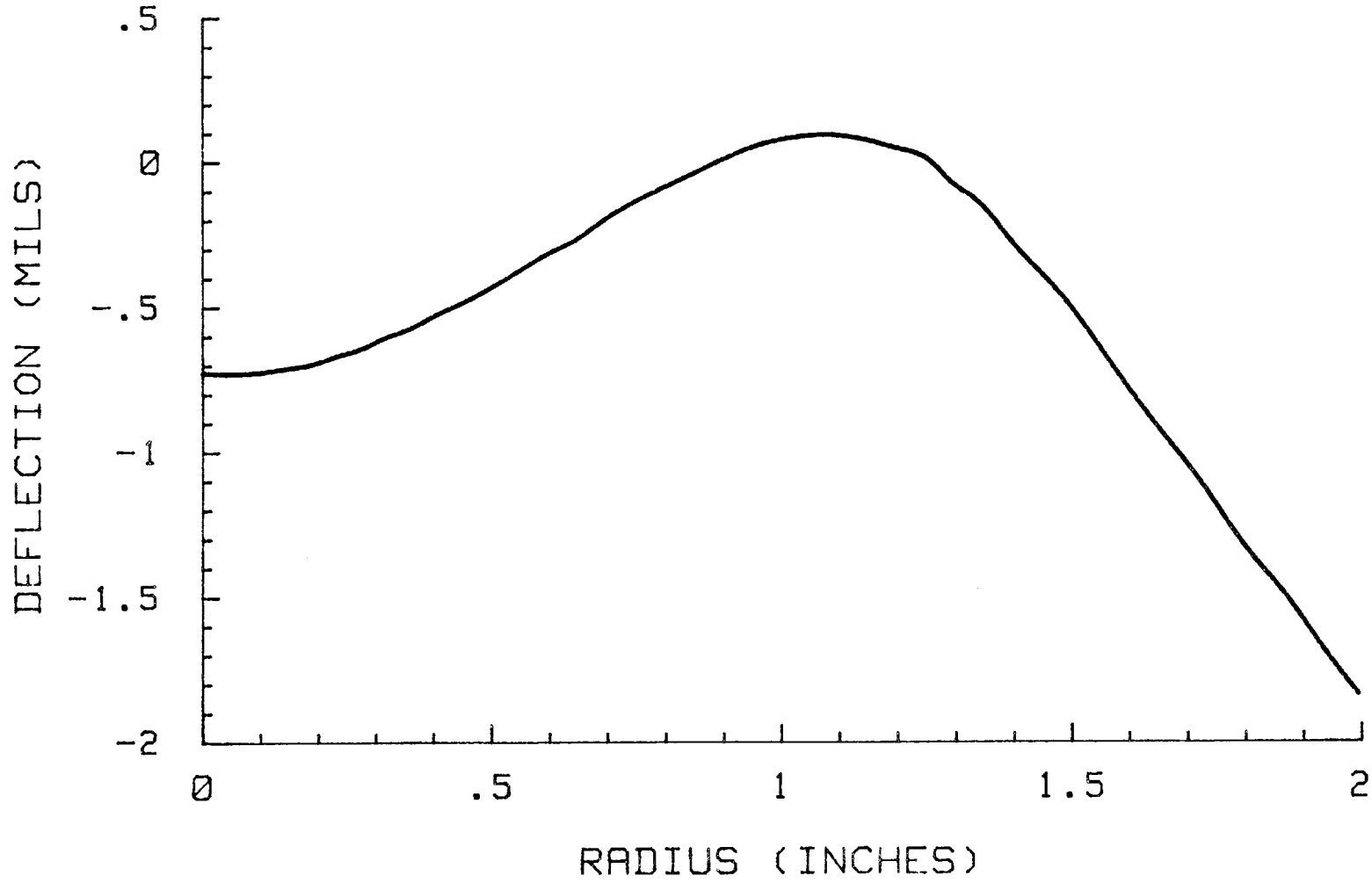

Figure 30. Validation of 3-D window structural model: Calculated window deflection for 3-D shell elements.

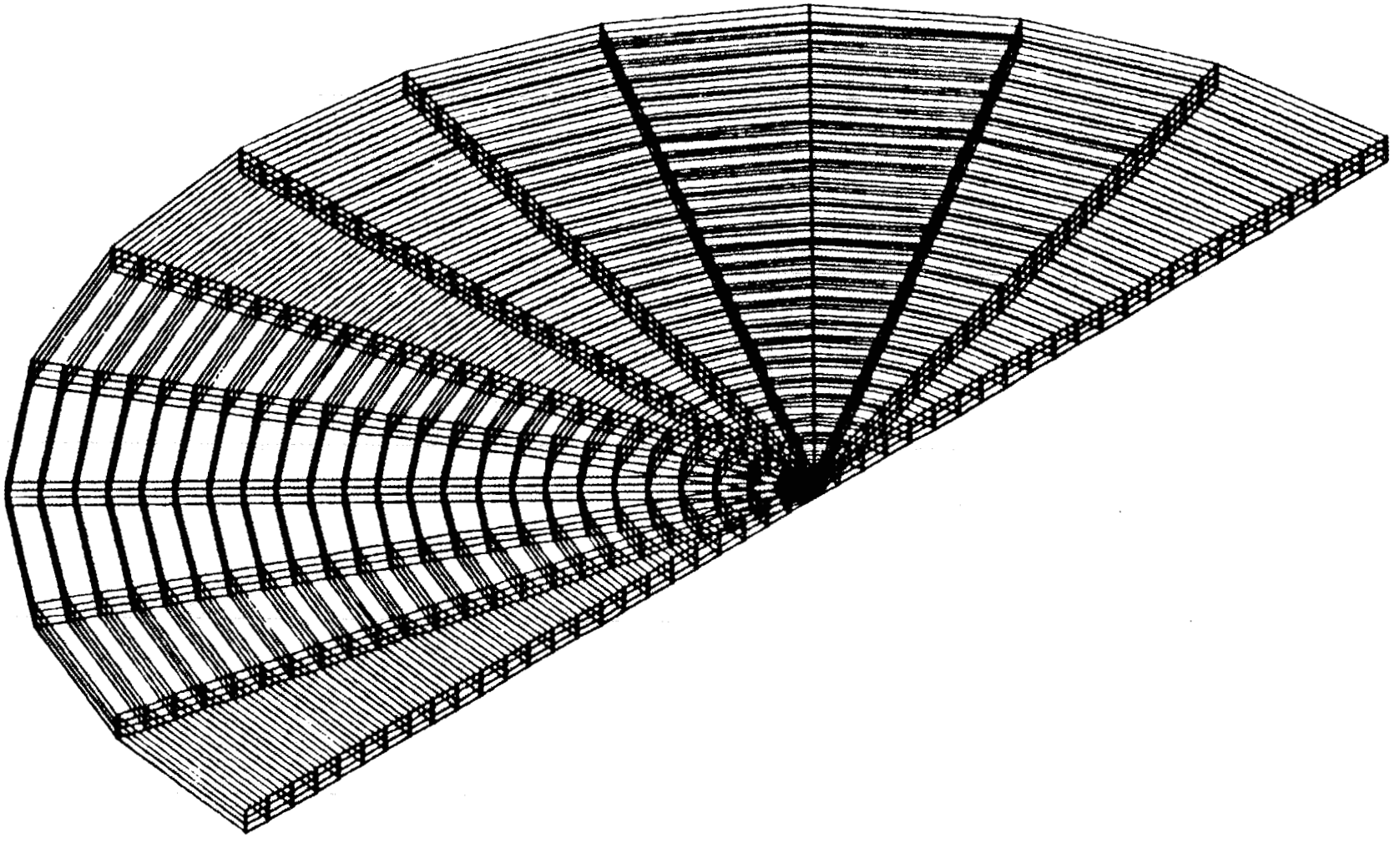

Figure 31. Finite element 3-D model for thermal analysis of the 140 GHz double-disc window.

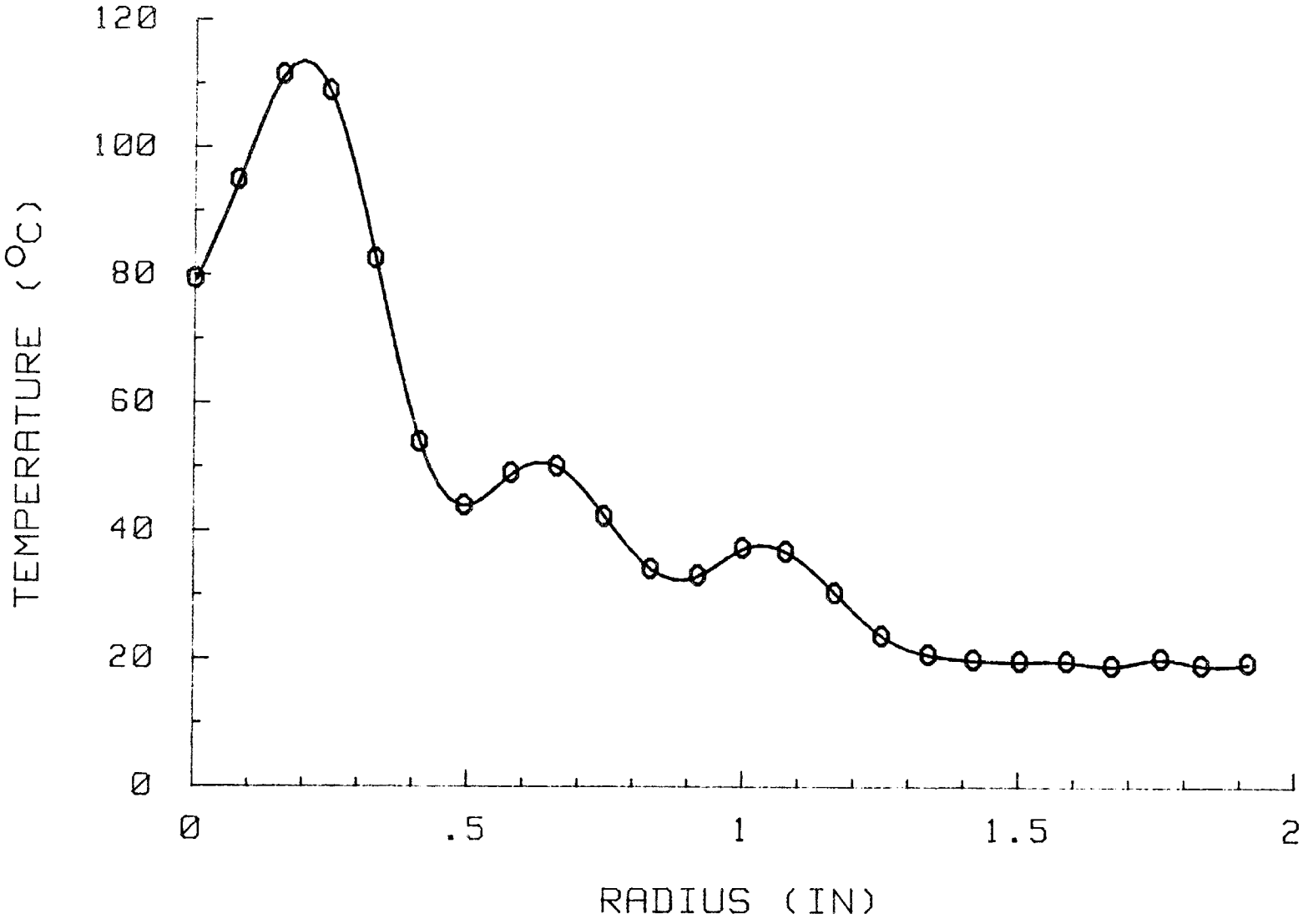

Figure 32. Double-disc window 3-D analysis: Temperature profile from center to inlet for the vacuum side of the window, 100 kW CW operation.

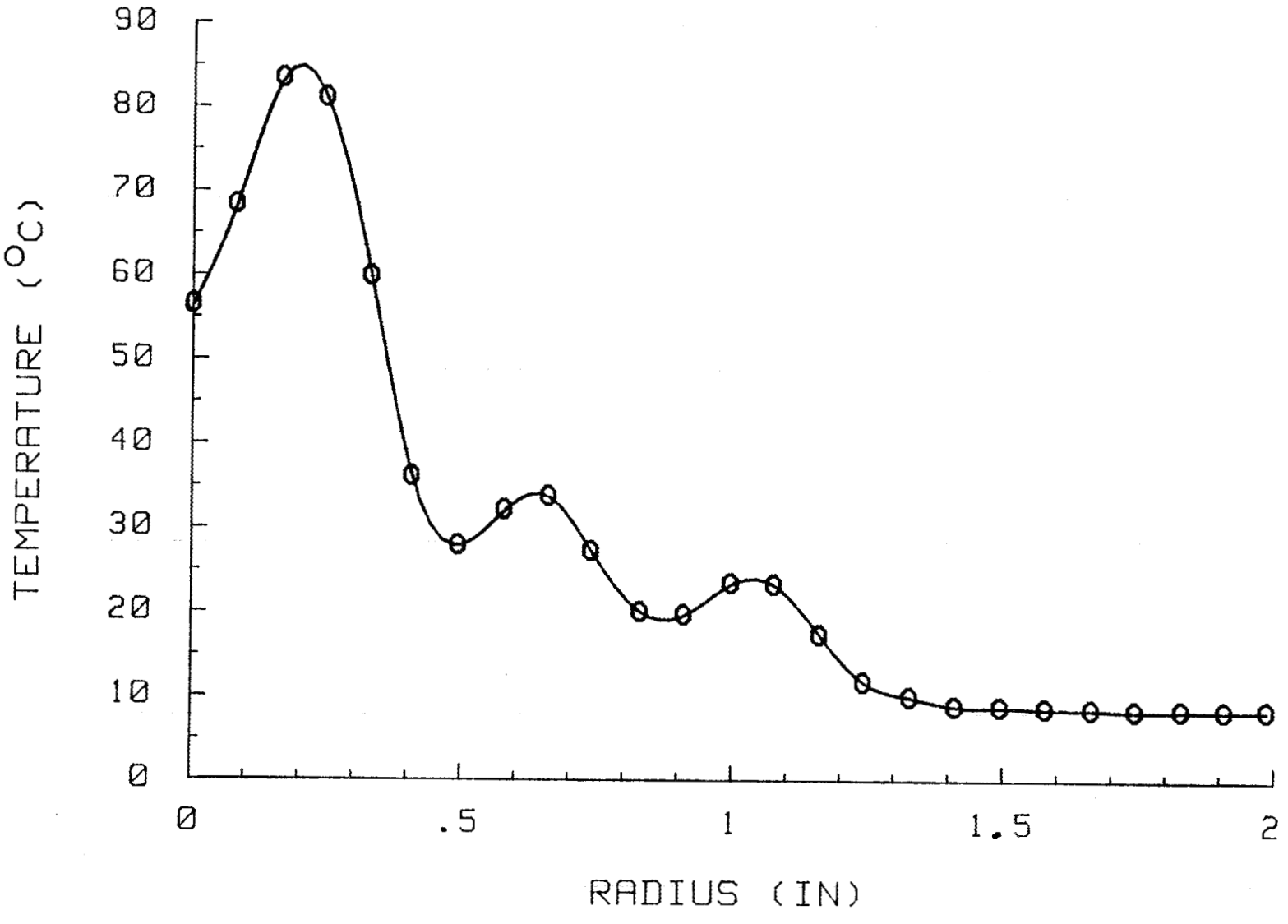

Figure 33. Double-disc window 3-D analysis: Temperature profile from center to inlet for the coolant side of the window, 100 kW CW operation.

Figure 34 shows the deformation of the finite element structure due to the distributed pressure load. Figures 35 and 36 show the displacement of the vacuum-side window disc due to pressure load only. The peak deflection is 0.0022" at the center of the window. Figure 35 gives the displacement profile moving out from the window center toward the coolant inlet, where the pressure is highest, so the window edge is actually deflected slightly downward from its unloaded position. However, at the coolant outlet, where the pressure is lower, the window deflects upward by 0.0005", as shown in Figure 36. Typical stress profiles for the pressure-only loads are given for the vacuum surface in Figure 37 and for the cooled surface in Figure 38. The peak tensile stress of 13.77 kpsi is less than 25% of the manufacturer's published value for the ultimate tensile strength of sapphire. A window deflection test using the design analyzed above is scheduled for next quarter. Results of these tests will be compared to the calculated stresses and deflections due to pressure-load only. This comparison will help validate the accuracy of our calculations.

Figure 39 shows the peak axial window deflection due to combined pressure and thermal stresses (i.e., with 100 kW CW power). The peak window deflection is 0.0028" or just slightly more than with pressure only. The stress distribution for the vacuum side of the window, from the window center to the coolant inlet, is given in Figure 40. The peak tensile stress is 14.3 kpsi. Figure 41 shows the stress profile for the coolant surface, where the peak tensile stress is 14.8 kpsi. These stress levels are probably sufficiently low to yield the desired window lifetime. Of course, because of the uncertainty inherent in the fracture strengths of brittle materials, it is always desirable to operate at as low a stress as possible. With this in mind, we continue to look for ways to reduce the peak operating tensile stresses.

In conclusion, for the sapphire double-disc window design, the peak temperatures and stresses appear acceptable. The deflection test will validate the structural model and give us insight about the uncertainities in the calculations. A high-speed flow check will verify the pressure drop

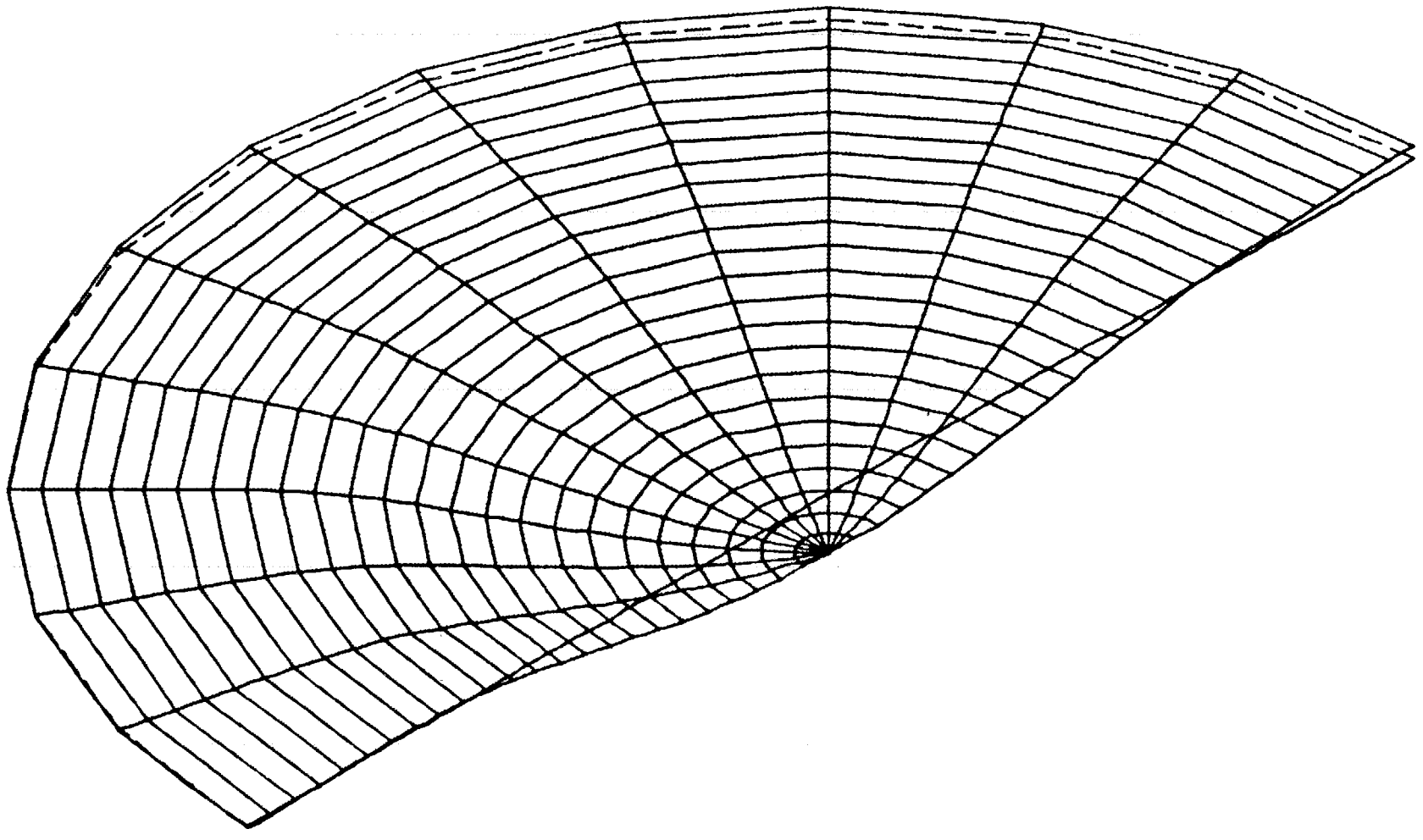

Figure 34. Axial deformation of a 3-D finite element structure for the 140 GHz window with pressure load only.

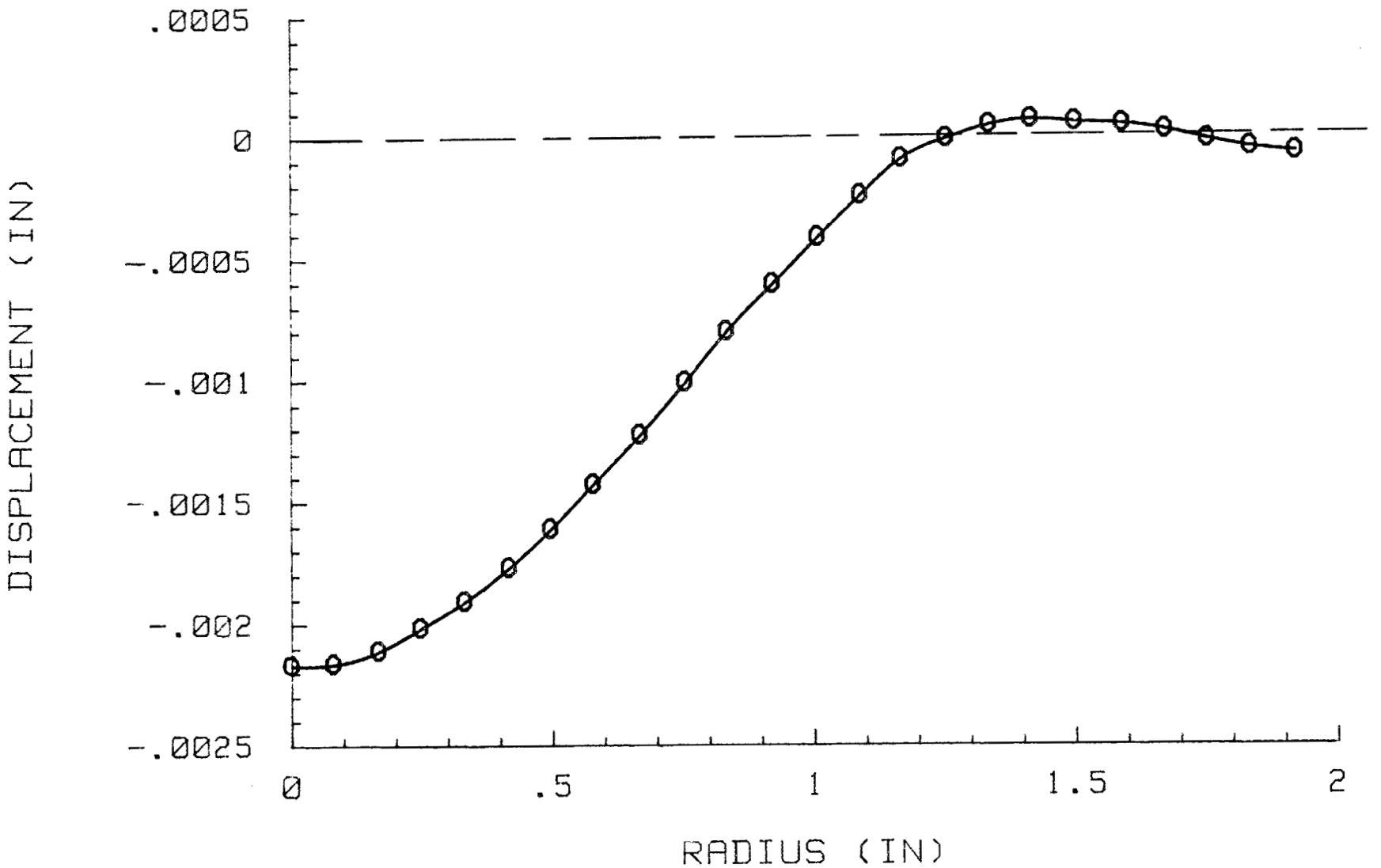

Figure 35. Double-disc window 3-D analysis: Displacement profile from center to inlet for the vacuum side of the window, pressure load only.

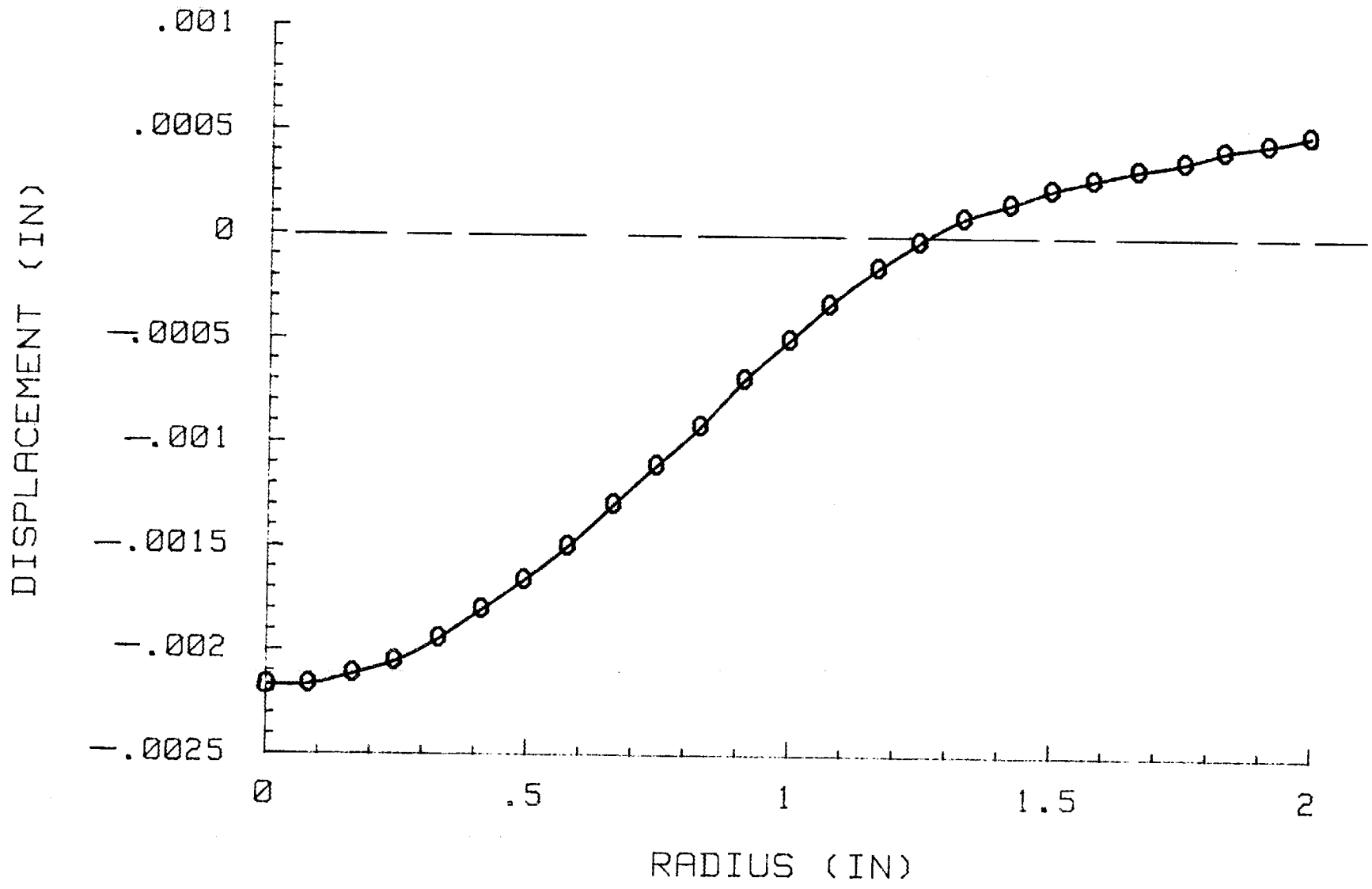

Figure 36. Double-disc window 3-D analysis: Displacement profile from center to outlet for the vacuum side of the window, pressure load only.

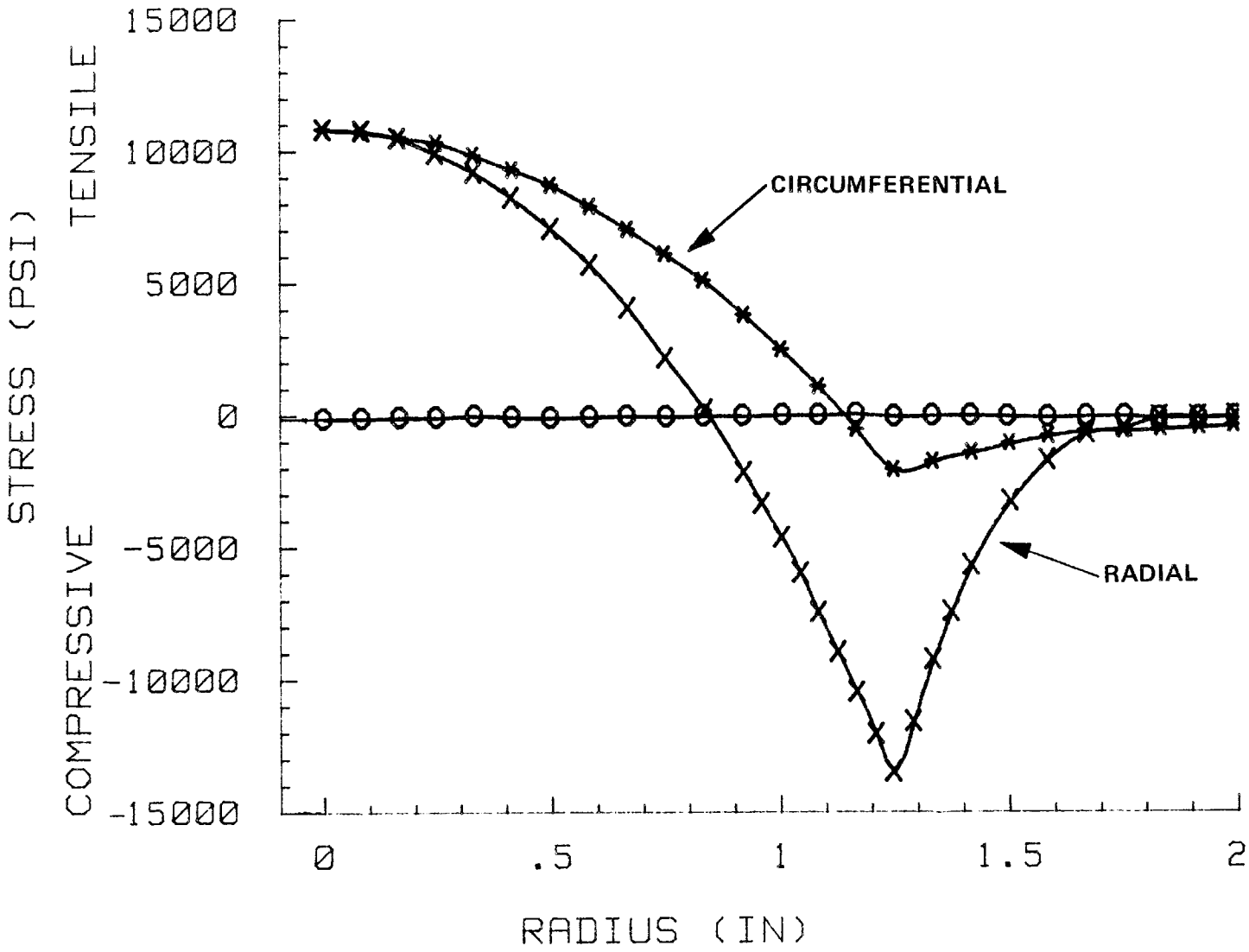

Figure 37. Double-disc window 3-D analysis: Stress profile from center to inlet for the vacuum side of the window, pressure load only.

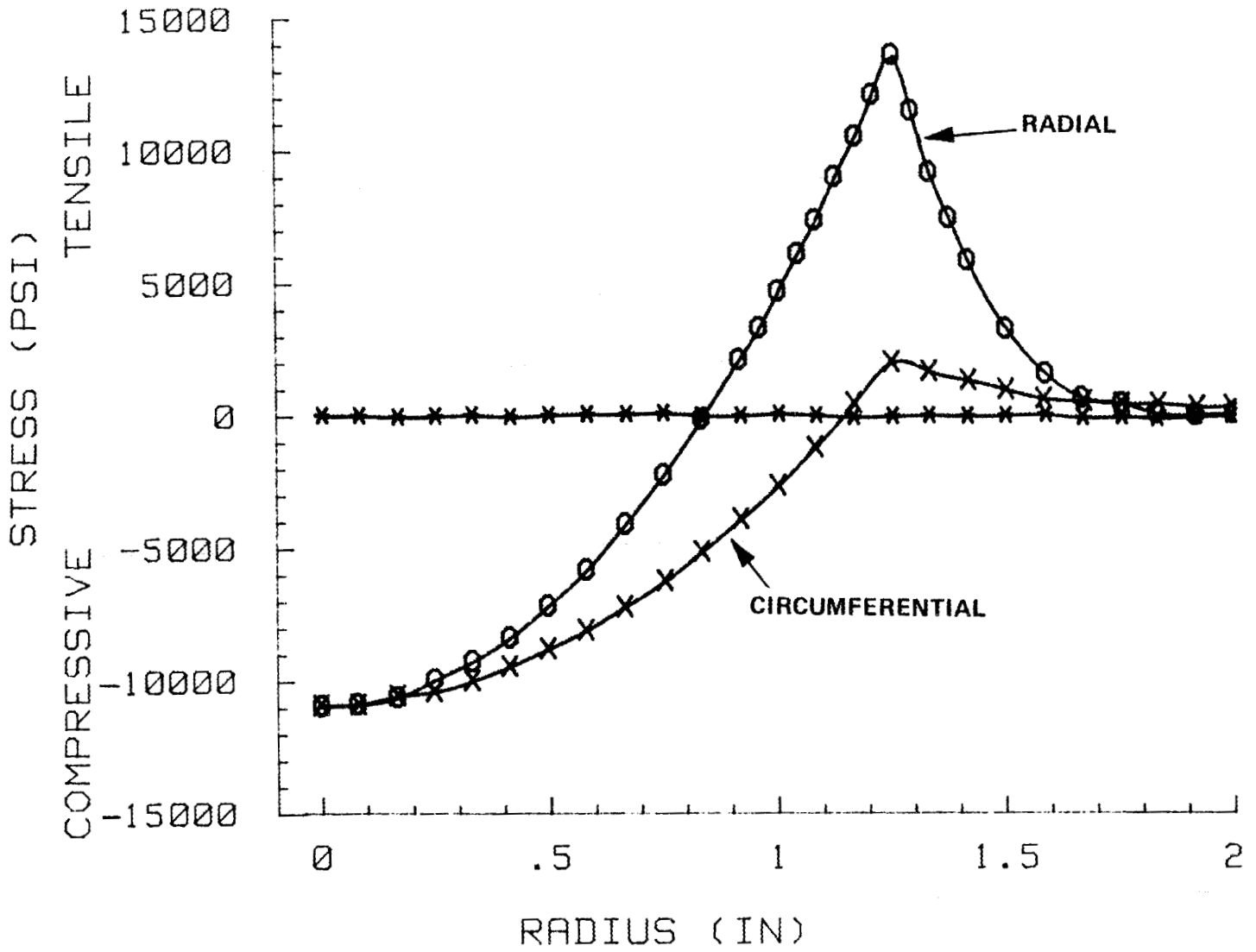

Figure 38. Double-disc window 3-D analysis: Stress profile from center to inlet for the coolant side of the window, pressure load only.

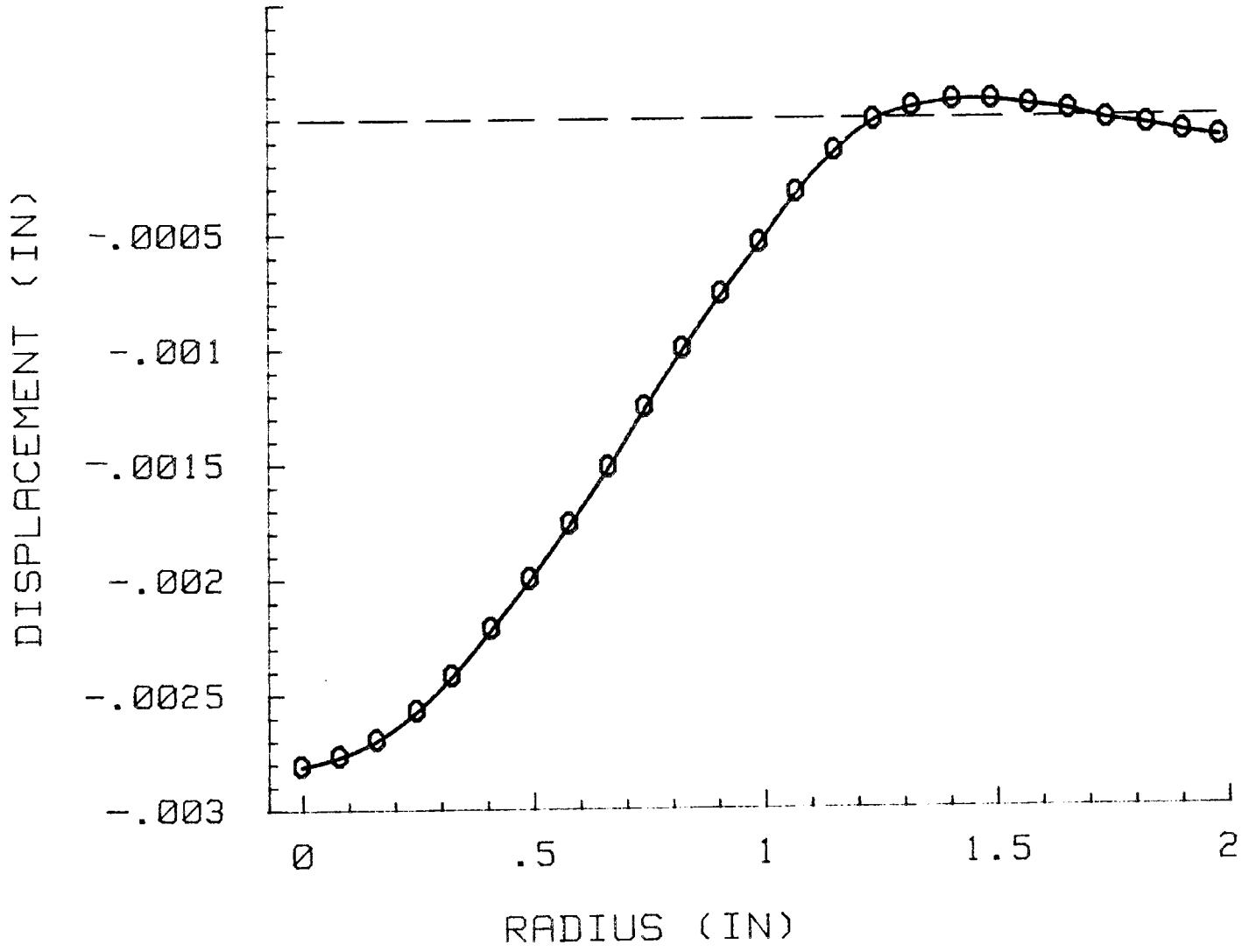

Figure 39. Double-disc window 3-D analysis: Deflection profile from center to inlet for the vacuum side of the window, 100 kW CW operation.

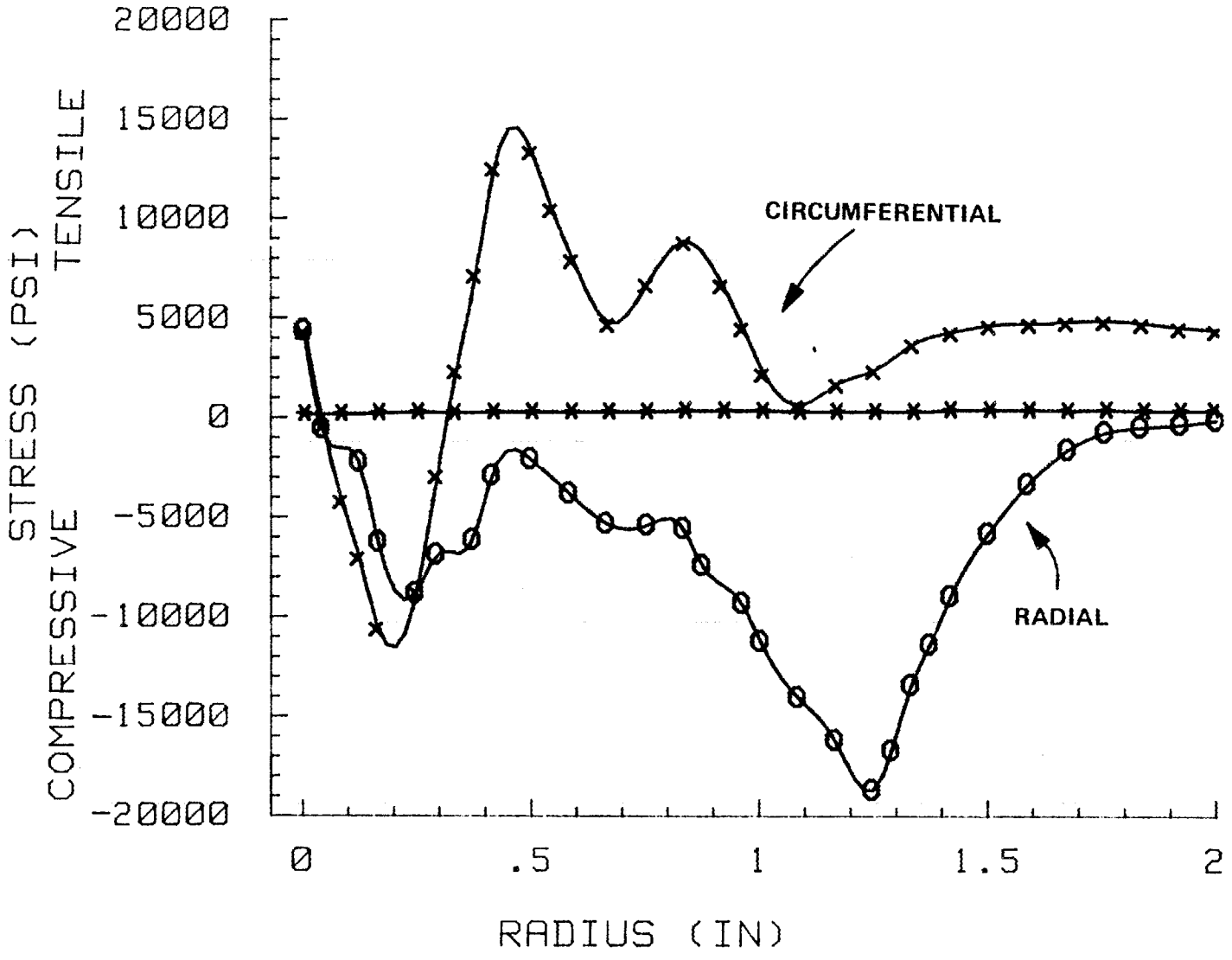

Figure 40. Double-disc window 3-D analysis: Stress profile from center to inlet for the vacuum side of the window, 100 kW CW operation.

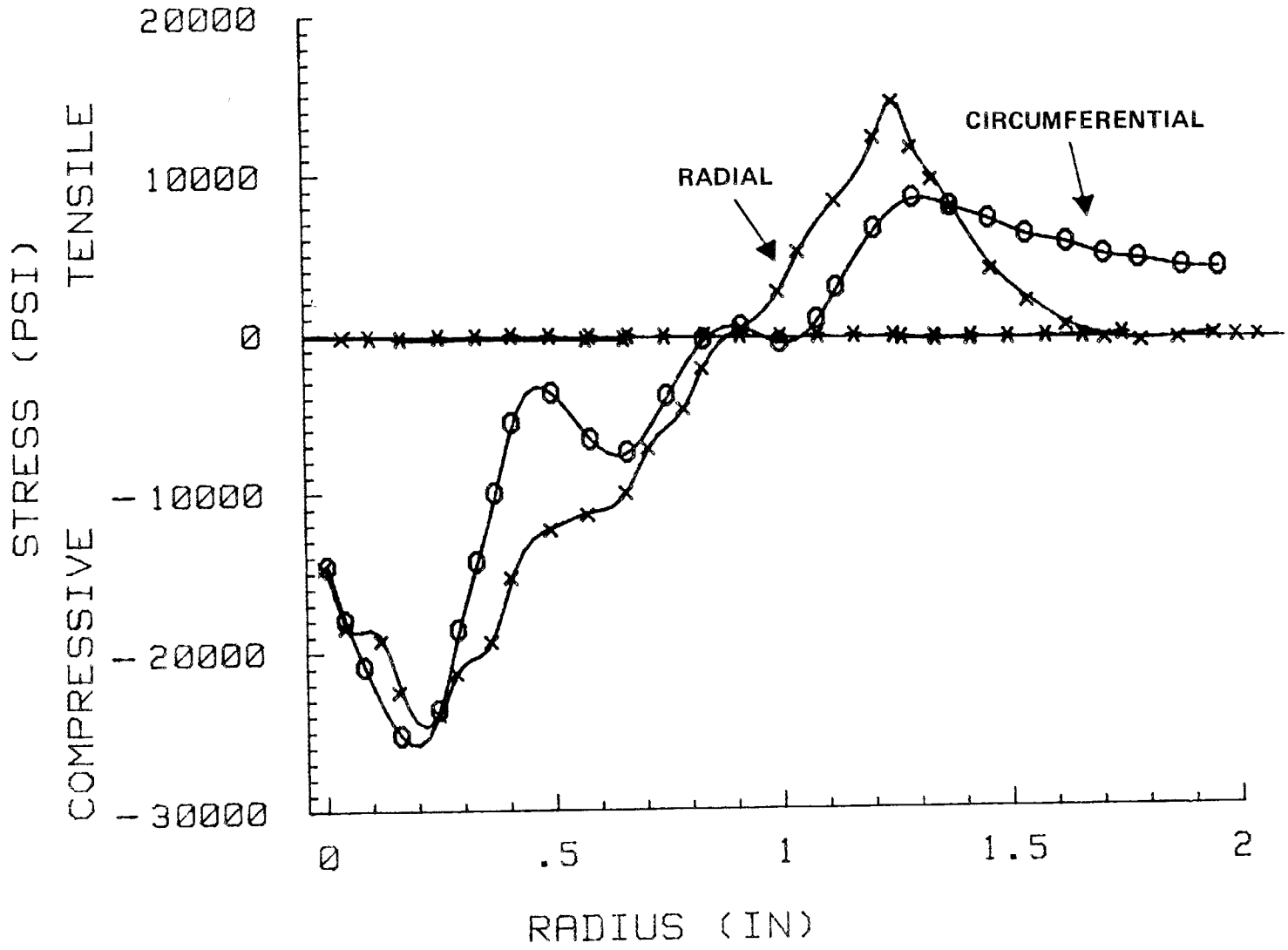

Figure 41. Double-disc window 3-D analysis: Stress profile from center to inlet for the coolant side of the window, 100 kW CW operation.

estimates. The use of the computer code FLUENT will allow optimization of the cooling flow pattern. We hope to obtain this computer code sometime next quarter.

B. DOUBLE-DISH WINDOWS

Several new geometries of "ultra-flat" dish windows have been created and analyzed for their ability to withstand pressure load. Previous calculations indicated that these ultra-flat dishes would have better microwave characteristics than more curved dishes. The critical buckling load for several ultra-flat dishes ranges from 45 to 120 psi. Unfortunately, the designs with higher buckling pressures have unacceptably high tensile stresses near the braze joint. Thus, further work is underway to determine a suitable compromise.

VI. SUPERCONDUCTING SOLENOID MAGNET SYSTEM

The designs of the two superconducting magnets were completed by two different vendors, both of whom initiated fabrication this quarter. Design reviews were held for both vendors. The final coil and cryostat designs were approved as being compatible with the 140 GHz gyrotron. We are closely monitoring the progress of the two vendors to ensure that the magnets arrive on schedule and that they fully comply with our specification.

A two-coil magnet design[1] was approved for use by both vendors. The three-coil design originally considered by one vendor,[1] was eliminated because of manufacturing problems and the technical risk involved. The magnet vendor felt it was possible to reach the full 6% taper requirement using a two-coil configuration. Initial study of the ramifications of a two-coil design indicated no adverse effects on the gyrotron design or operation. Because of the increased safety margin of the two-coil design, the decision was reached to use this design for both magnet systems on order.

Design reviews were held for both vendors this quarter. The purpose of the reviews was to make certain that the magnet designs were compatible with the 140 GHz gyrotron and the Varian test set. The coil designs were evaluated at Varian and found to be compatible with our present gun design. The cryostat dimensions were checked to make sure that they would fit in our existing socket. A diagram of the general dewar configuration is given in Figure 42. This configuration is a compromise to obtain the desired helium hold time and also fit in our existing test set. The dewar design for the final end-users may be different than this design. At the completion of the design reviews, fabrication start-up was authorized for both vendors.

Since the magnet is critical in order to test the first tube, we are monitoring the progress of the magnets quite closely. Our follow-up effort consists of close telephone contact with the project engineer and frequent unannounced visits at the vendor site. In addition, both vendors are required to submit monthly reports to summarize their progress. So far,

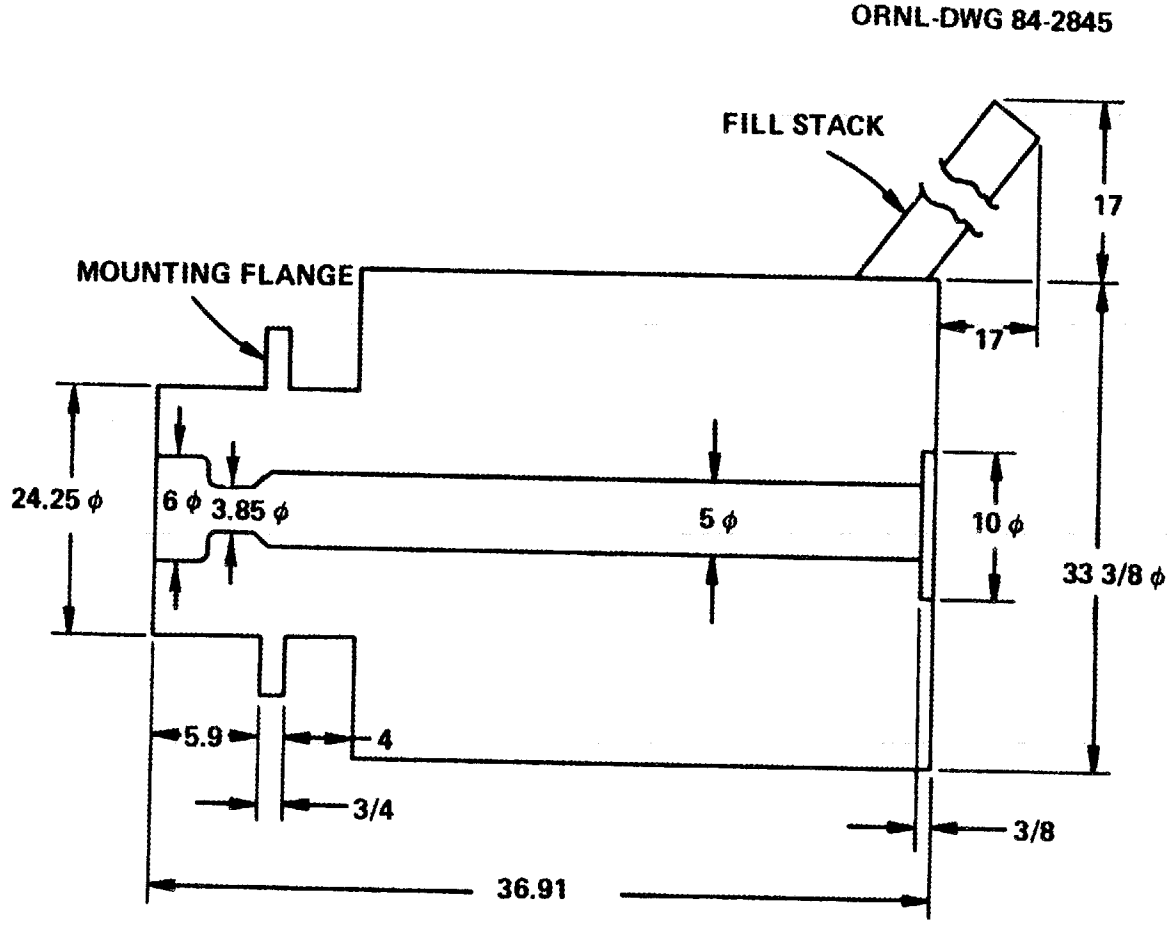

Figure 42. 140 GHz magnet dewar layout. Dimensions shown are in inches.

both magnets are on schedule and both vendors anticipate an on-time delivery.

Another important aspect of a successful magnet system is the quality assurance plan. Figure 43 is a block diagram of the manufacturing flow for a superconducting magnet system. Noted underneath each block is the quality assurance inspection or test which helps to ensure that the specification is being met. The final acceptance test is the ultimate criteria for documenting specification compliance. Every aspect of the magnet system is fully checked to ensure satisfactory operation. Both vendors anticipate submitting the acceptance test plan for approval early in the next quarter.

In summary, both vendors were reviewed this quarter and fabrication was initiated. A decision was reached to drop the three-coil approach in favor of two-coil designs for both systems. No adverse affects on the gyrotron performance are anticipated as a result of this decision. Our extensive follow-up on vendor progress has concentrated on ensuring on-time delivery of a quality magnet system. The drafting of an acceptance test plan has been initiated by both vendors.

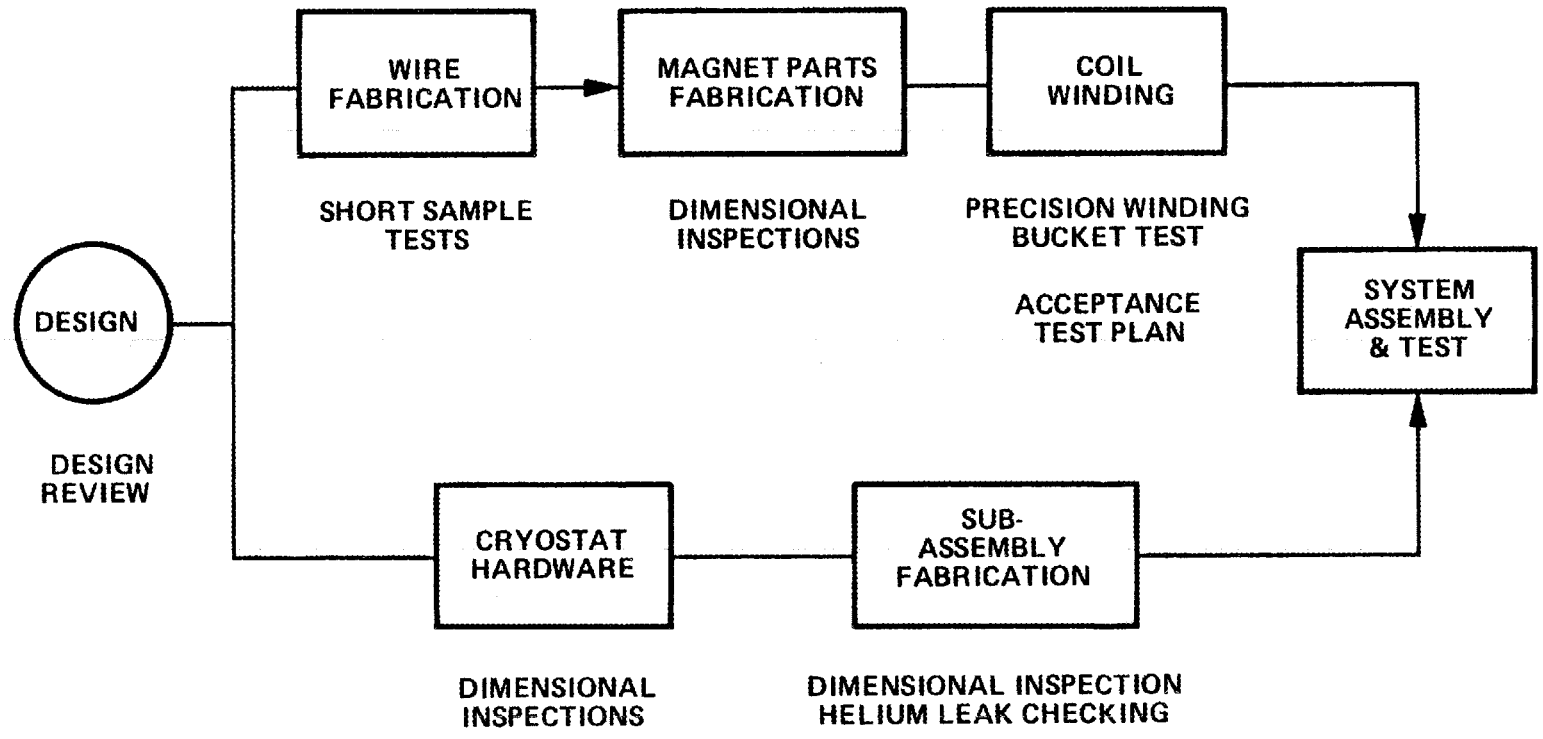

Figure 43. Superconducting solenoid manufacturing process.

VII. 140 GHz COMPONENTS, DIAGNOSTICS AND PROTECTIVE DEVICES

A. WATERLOAD

The electromagnetic radial divertor (ERD) waterload has been ordered. Parts fabrication is nearly complete. Assembly should begin next quarter.

B. INFRARED DIAGNOSTICS

The 140 GHz IR grid has been ordered. Tests of a grid which has been scaled to 60 GHz will be performed next quarter on a 60 GHz pulse tube.

The IR system software package from Thermoteknix (purchased from AGA Corporation), which translates intensity measurements to temperature, was recently improved. The upgraded software package permits the use of filters in the optical path. A variety of calibration tests will be performed next quarter. Additional software requirements to account for the transmission function and temperature of the grid are presently being evaluated for a price quote by Thermoteknix.

C. MODE FILTER

Most of the effort during this period was on an alternate helical mode filter, discussed in the previous report.[1] The design employs a very shallow helix having several turns per inch with a half-wavelength spacing. Titanium dioxide is planned for the loss material.

Samples of both titanium dioxide and barium titanate have been successfully machined in our shop. No problems with the final machining operation are anticipated. A vendor, with plasma-spray guns small enough to get inside the 2-1/2" diameter, has been identified. Use of such small plasma guns should enable complete coverage in the grooves. Initial machining has been completed. This includes cutting the helix and fabricating all the parts that need to be brazed.

D. ARC DETECTOR/FREQUENCY SAMPLER

Drawings have been started for the VGT-8014 arc detector frequency sampler. As noted in the last report, a second light pipe has been incorporated in the design.[1]

There is some concern that the light-sensing arc detector may see fluorescence from inside the tube through the transparent sapphire window, thereby causing false crowbars. If this occurs, an alternate method would be to use an audio arc detector, such as the one used by ORNL in a 28 GHz system. Prints of this detection system have been received from ORNL. It is planned to have one of the audio arc detectors ready for the first tube test.

Two different techniques of transferring the rf signal from the frequency sampler to the test console have been considered. In the first case, the transmission is in the TE^{o}_{11} mode. This requires two TE_{10} to TE^{o}_{11} transitions and appropriate tapers. In the second case, the power is transmitted in the TE^{o}_{01} mode. This is the lowest loss case. This requires two TE_{10} to TE^{o}_{01} transitions and appropriate tapers. Both techniques will probably be tested on the first tube.

E. DIRECTIONAL COUPLER

Efforts during the third quarter concentrated primarily on finding a machine shop capable of constructing the 35 GHz test coupler described in the previous quarterly report.[1] The size and desired construction tolerances made it difficult to locate a shop with the required equipment and expertise. Drawings for the coupler were completed and copies sent to the only two shops that could be found with the equipment capable of machining over the required 59" length. Of these, only the University of California, San Diego Upper Campus Machine Shop has expressed a willingness to undertake the construction, providing that certain tolerances are relaxed. Critical dimensions had been specified to less than 0.001".

The inability to locate a shop capable of manufacture at the desired tolerances forced relaxation to $\pm$0.001". Since the effect of the coupling holes on phase velocity in the respective guides is not considered in the calculations, the 35 GHz test coupler was designed to be adjustable to five different depths of the rectangular guide, each symmetrically spaced 0.001" apart around the calculated ideal depth. Cold test measurements on this coupler will be used to ascertain the effect of the coupling holes for use in the 140 GHz design.

At this point, the drawings are being redone to reflect the relaxed tolerances and sent to the UCSD shop for a quote. The UCSD shop has considerable experience in this type of construction and builds couplers used at Lawrence Livermore National Laboratories.

VIII. PROGRAM SCHEDULE AND PLANS FOR NEXT QUARTER

The designs of the first two experimental tubes, Experimental Tube 1 and Preprototype Tube 1, are essentially complete and the manufacture of Experimental Tube 1 is well underway. The fabriction of gyrotron magnets at two different vendors is being monitored closely to ensure timely delilvery of the magnets. Gyrotron components, diagnostics, and protective devices are being manufactured in preparation for the first tube tests. As indicated by the milestone chart for the 140 GHz Gyrotron Development Program in Figure 44, tests on the first tube are still planned for the end of next quarter.

During the next quarter, the following tasks will be performed:

Slight modifications in the design of, both, the simple TE_{031} cavity and the TE_{021}/TE_{031} complex cavity will be made to try to decrease back-rf leakage and output mode conversion. Successful modifications will be incorporated into the earliest possible experimental vehicles.

A sensitivity analysis will be performed for the TE_{021}/TE_{031} complex cavity using the results of the plastic/elastic stress analysis performed this quarter. This analysis will determine if thermally induced deformations of the cavity walls will cause deleterious changes in the electrical characterisics of the cavity. Fatigue calculations will be carried out for the TE_{021}/TE_{031} cavity design for cavities made from AL-15 copper and OFHC copper. Cold tests of the simple TE_{031} cavity designs will be performed.

Further cold tests of the beam tunnel structure and additional temperature and stress calculations for the second lossy ring in the beam tunnel will be carried out.

The two superconducting magnet systems will be constructed and tested.

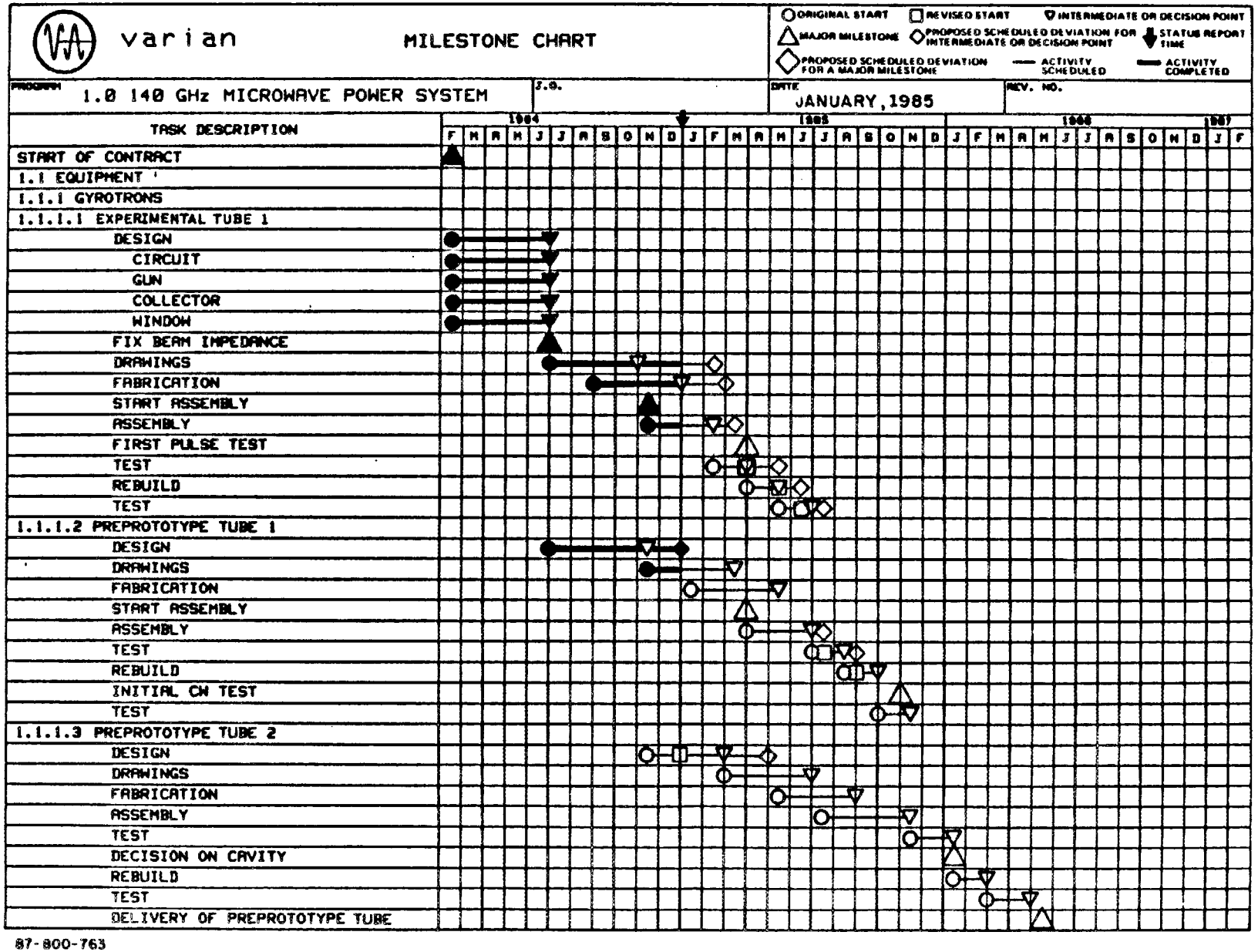
varian
MILESTONE CHART
ORIGINAL START
REVISED START
INTERMEDIATE OR DECISION POINT
MAJOR MILESTONE
PROPOSED SCHEDULED DEVIATION FOR INTERMEDIATE OR DECISION POINT
STATUS REPORT TIME
PROPOSED SCHEDULED DEVIATION FOR A MAJOR MILESTONE
ACTIVITY SCHEDULED
ACTIVITY COMPLETED
PROGRAM
1.0 140 GHz MICROWAVE POWER SYSTEM
J.O.
DATE
JANUARY, 1985
REV. NO.
TASK DESCRIPTION
1984
1985
1986
1987
F M A M J J A S O N D J F M A M J J A S O N D J F M A M J J A S O N D J F
START OF CONTRACT
1.1 EQUIPMENT
1.1.1 GYROTRONS
1.1.1.1 EXPERIMENTAL TUBE 1
DESIGN
CIRCUIT
GUN
COLLECTOR
WINDOW
FIX BEAM IMPEDANCE
DRAWINGS
FABRICATION
START ASSEMBLY
ASSEMBLY
FIRST PULSE TEST
TEST
REBUILD
TEST
1.1.1.2 PREPROTOTYPE TUBE 1
DESIGN
DRAWINGS
FABRICATION
START ASSEMBLY
ASSEMBLY
TEST
REBUILD
INITIAL CW TEST
TEST
1.1.1.3 PREPROTOTYPE TUBE 2
DESIGN
DRAWINGS
FABRICATION
ASSEMBLY
TEST
DECISION ON CAVITY
REBUILD
TEST
DELIVERY OF PREPROTOTYPE TUBE
87-800-763

Figure 44.

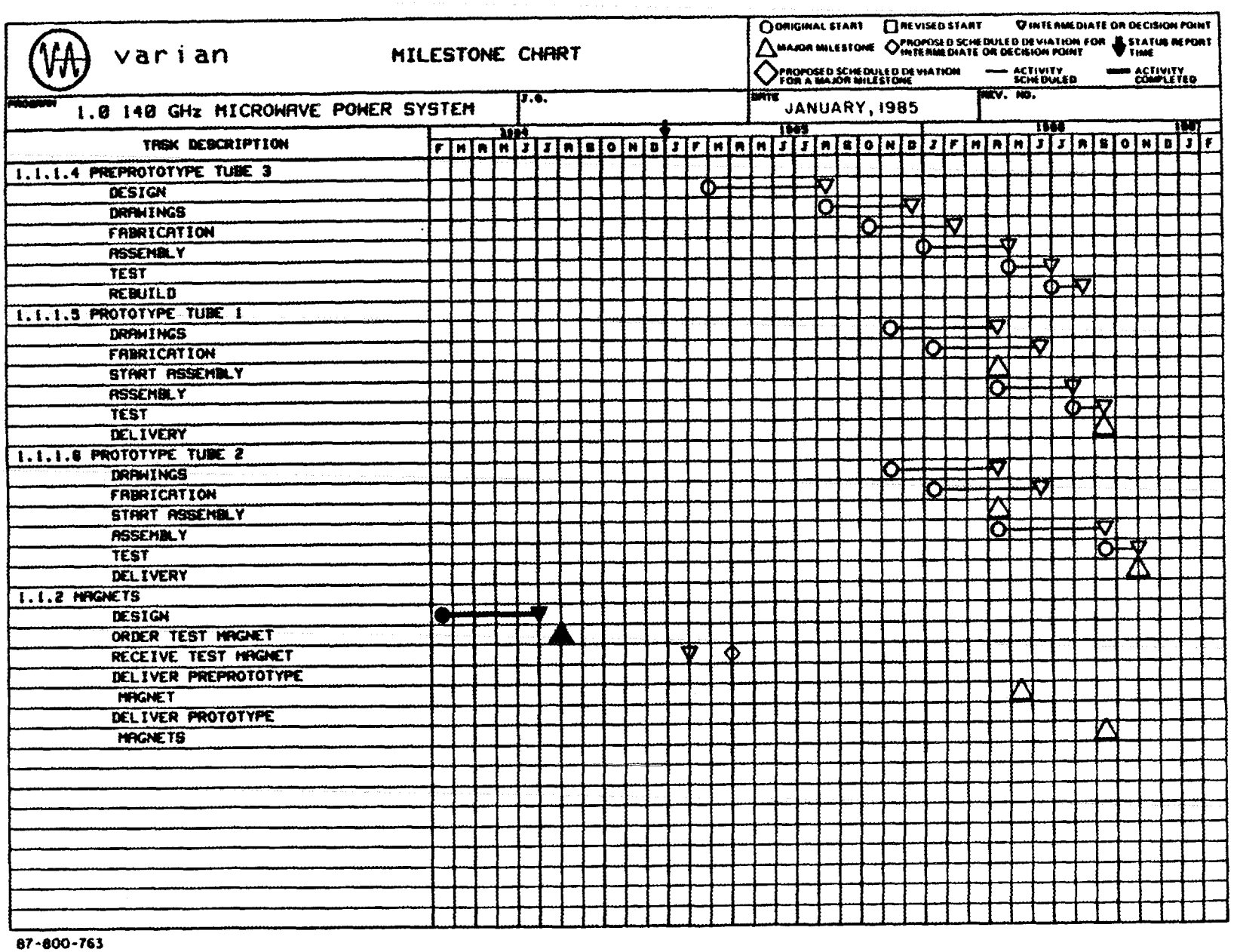

87-800-763

Figure 44. (Continued)

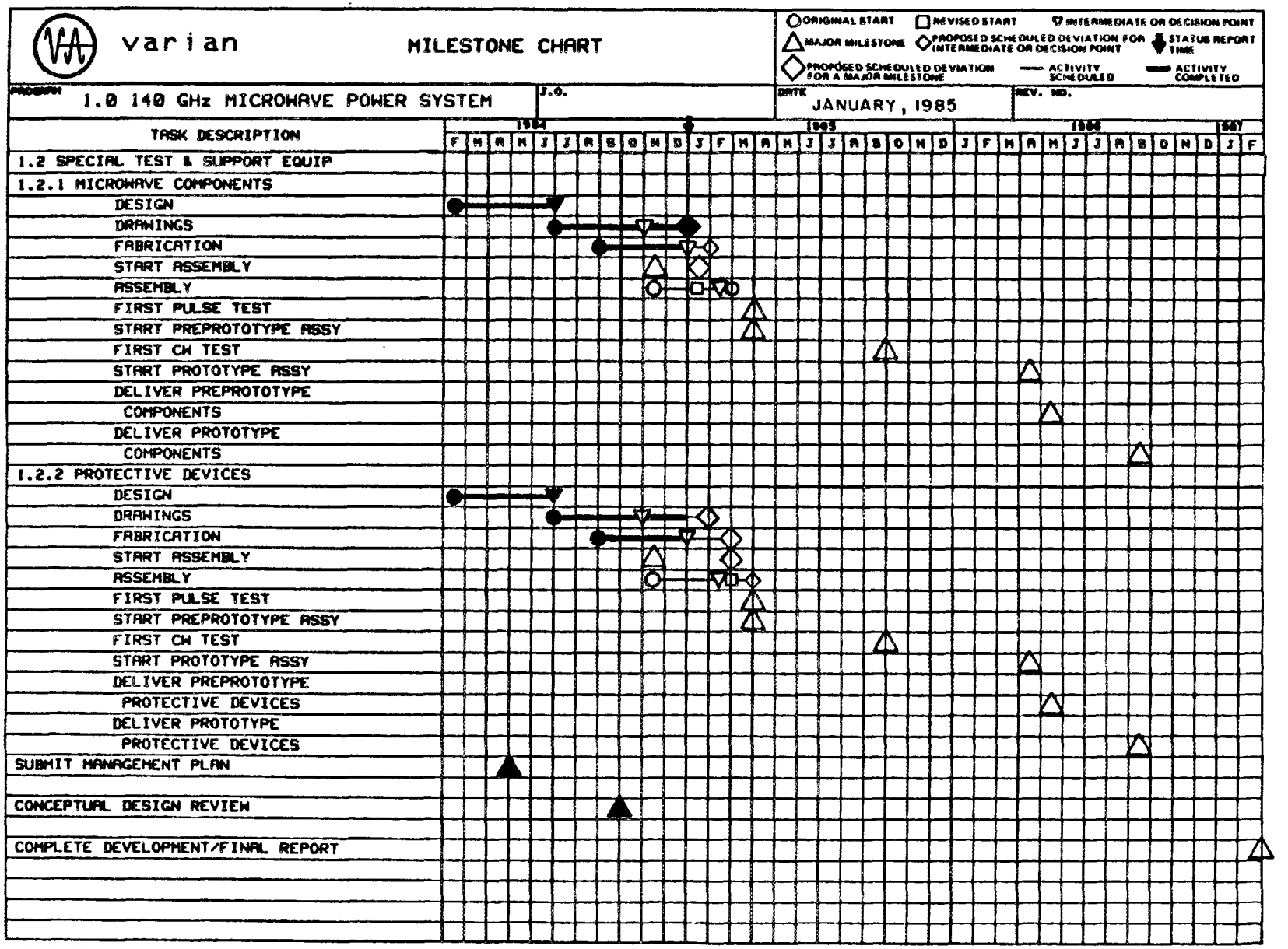

87-800-763

Figure 44. (Continued)

All components, diagnostics, and protective devices needed for tests on the first experimental tube will be completed and readied for test.

Fabrication of the 35 GHz test directional coupler will begin.

Pulse tests on the first experimental tube are scheduled to begin in March, 1985.

REFERENCES

1. K. L. Felch, et. al., "140 GHz Gyrotron Development Program", Quarterly Report No. 2, July through September 1984, prepared by Varian Associates, Inc., under Subconstract Purchase Order No. 55Y-95128C for Oak Ridge National Laboratory operated by Martin Marietta Energy Systems, Inc. for the U.S. Department of Energy, under Prime Contract DE-AC05-840R21400.

2. K. Felch, et. al., "Design and Operation of Magnetron Injection Guns for a 140 GHz Gyrotron", Int. Electron Devices Meeting - Technical Digest, pp. 362-365, San Francisco, Dec. 1982.

3. K. L. Felch, et. al., "140 GHz Gyrotron Development Program", Quarterly Report No. 1, March through June 1984, prepared by Varian Associates, Inc., under Subcontract Purchase Order No. 55Y-95128C for Oak Ridge National Laboratory operated by Martin Marietta Energy Systems, Inc. for the U.S. Department of Energy, under Prime Contract DE-AC05-840R21400.

4. Personal communication, Dr. W.W. Ho.

5. K. Felch, et. al., "A 60 GHz, 200 kW CW, Gyrotron with a Pure Output Mode", Int. J. Electronics, pp. 815-820, Vol. 57, No. 6, Dec. 1984.

ORNL/Sub/55Y-95128C/1
July 1984

INTERNAL DISTRIBUTION

1. P. F. Becher
2. L. A. Berry
3. T. S. Bigelow
4. J. M. Galyon
5. H. H. Haselton
6-8. G. R. Haste
9. H. D. Kimrey, Jr.
10. R. P. Jernigan
11. H. C. McCurdy
12. D. H. Metzler
13. O. B. Morgan
14. J. Sheffield
15. T. L. White
16-17. Laboratory Records Department
18. Laboratory Records, ORNL-RC
19. Y-12 Document Reference Section
20-21. Central Research Library
22. Fusion Energy Division Library
23. Fusion Energy Division Publications Office
24. ORNL Patent Office, ATTN: J. M. Spicer

EXTERNAL DISTRIBUTION

25. M. N. Asfar, Francis Bitter National Magnet Laboratory, Massachusetts Institute of Technology, Cambridge, MA 02139
26. D. S. Beard, Office of Fusion Energy, Office of Energy Research, ER-531 GTN, U. S. Department of Energy, Washington, DC 20545
27. N. Bowen, Princeton University, Plasma Physics Laboratory, P.O. Box 451, Princeton, NJ 08540
28. R. A. Dandl, AMPC, Inc., 2210 Encinitas Blvd. Suite P, Encinitas, CA 92024
29. J. F. Decker, Office Fusion Energy, Office of Energy Research, ER-1, GTN, U. S. Department of Energy, Washington, DC 20545
30. N. J. Dionne, Raytheon Co., Microwave and Power Tube Division, Waltham, MA 02254
31. W. Friz, AFAL/DHM, Wright Patterson AFB, OH 45433
32. T. V. George, Office of Fusion Energy, Office of Energy Research, ER-531, GTN, U. S. Department of Energy, Washington, DC 20545
33. T. Godlove, Office of Energy Research, ER-20, GTN, U. S. Department of Energy, Washington, DC 20545
34. M. J. Gouge, U. S. Department of Energy, Oak Ridge Operation, P. O. Box E, Oak Ridge, TN 37831
35. V. J. Granatstein, Naval Research Laboratory, Code 6740, Washington, DC 20545
36. G. M. Haas, Office of Fusion Energy, Office of Energy Research, ER-533, GTN, U. S. Department of Energy, Washington, DC 20545
37. J. L. Hirshfield, Yale University, Department of Engineering and Applied Science, P. O. Box 2159, Yale Station, New Haven, CT 06520
38. W. W. Ho, Rockwell International Science Center, 1049 Camino dos Rios, Thousand Oaks, CA 91360
39. H. Hsuan, Plasma Physics Laboratory, Princeton University, P. O. Box 451, Princeton, NJ 08544
40. K. Krause, MFE Electronics Engineering Department, Lawrence Livermore National Laboratory, P. O. Box 5511 (L-634), Livermore, CA 94550
41. J. V. Lebacqz, Stanford Linear Accelerator Center, Stanford University, P. O. Box 4349, Stanford, CA 94305
42. C. M. Loring, Varian Associates, Inc., EIMAC Division, 301 Industrial Way, San Carlos, CA 94070

43. C. P. Moeller, GA Technologies, Inc., Fusion and Advanced Technology, P. O. Box 85608, San Diego, CA 92138
44. R. Prater, GA Technologies, Inc., Fusion and Advanced Technology, P. O. Box 85608, San Diego, CA 92138
45. R. Profant, Office of Nuclear Materials Production, DP 13.2, GTN, U. S. Department of Energy, Washington, DC 20545
46. M. E. Read, Naval Research Laboratory, Code 6740, Washington, DC 20375
47. D. B. Remsen, GA Technologies, Inc., Fusion and Advanced Technology, P. O. Box 85608, San Diego, CA 92138
48. T. E. Romesser, TRW, 1 Spack Park, Bldg. R-1, Room 2044, Redondo Beach, CA 90278
49. G. Simonis, Harry Diamond Laboratory, 2800 Powder Mill Road, Adelphi, MD 20783
50. M. S. Sparks, Science Research Center, 9507 High Ridge Place, Beverly Hills, CA 90210
51. B. L. Stallard, Lawrence Livermore Laboratory, P. O. Box 5511 (L-637), Livermore, CA 94550
52. H. S. Staten, Office of Fusion Energy, Office of Energy Research, ER-531, GTN, U. S. Department of Energy, Washington, DC 20545
53. M. A. Stroscio, AFOSR, Bolling Air Force Base, Washington, DC 20332
54. R. S. Symons, Litton Industries Inc., Electron Tube Division, 960 Industrial Road, San Carlos, CA 94070
55. P. J. Tallerico, AT-5, Accelerator Technology Division, Los Alamos Scientific Laboratory, MS 821, P. O. Box 1663, Los Alamos, NM 87545
56. J. J. Tancredi, Hughes Aircraft Company, Electron Dynamics Division, 3100 W. Lomita Blvd., Torrance, CA 90509
57. R. J. Temkin, Plasma Fusion Center, Massachusetts Institue of Technology, 167 Albany Street AW16-254, Cambridge, MA 02139
58. Director, U. S. Army Ballistic Missle Defense Advance Technology Center, ATTEN: D. Schenk, ATC-R, P. O. Box 1500, Huntsville, AL 35807
59. Office of Assistant Manager for Energy Research and Development, Oak Ridge Operations Office, Department of Energy, Oak Ridge, TN 37831

VARIAN DISTRIBUTION

60.	R. Berry
61.	R. Bier
62-68.	J.E. Camp
69.	M. Caplan
70.	L.J. Craig
71.	K.L. Felch
72.	L.J. Fox
73-75.	C.R. Frazer
76.	H. Huey
77.	G. Huffman
78.	R.L. Ives
79.	H.R. Jory
80.	D. Latshaw
81.	E. Lien
82.	N. Lopez
83.	J.F. Moran
84.	J. Nielson
85.	D. Pirkle
86.	J.F. Shively
87.	S.T. Spang
88-89.	A. Staprans
90.	Technical Library